Pulse Propagation Effects in Optical 2D Fourier-Transform Spectroscopy: Theory

Austin P. Spencer,[†] Hebin Li,[‡,¶] Steven T. Cundiff,[‡] and David M. Jonas[*,†]

Department of Chemistry and Biochemistry, University of Colorado, Boulder, Colorado 80309-0215, JILA, University of Colorado and National Institute of Standards and Technology, Boulder, Colorado 80309-0440, and Department of Physics, Florida International University, Miami, Florida 33199

E-mail: david.jonas@colorado.edu

[*]To whom correspondence should be addressed
[†]University of Colorado Boulder
[‡]University of Colorado and National Institute of Standards and Technology
[¶]Florida International University

Abstract

A solution to Maxwell's equations in the three-dimensional frequency domain is used to calculate rephasing two-dimensional Fourier transform (2DFT) spectra of the D_2 line of atomic rubidium vapor in argon buffer gas. Experimental distortions from the spatial propagation of pulses through the sample are simulated in 2DFT spectra calculated for the homogeneous Bloch lineshape model. Spectral features that appear at optical densities of up to 3 are investigated. As optical density increases, absorptive and dispersive distortions start with peak shape broadening, progress to peak splitting, and ultimately result in a previously unexplored coherent transient twisting of the split peaks. In contrast to the low optical density limit, where the 2D peak shape for the Bloch model depends only on the total dephasing time, these distortions of the 2D peak shape at finite optical density vary with the waiting time and the excited state lifetime through coherent transient effects. Experiment-specific conditions are explored, demonstrating the effects of varying beam overlap within the sample and of pseudo–time domain filtering. For beam overlap starting at the sample entrance, decreasing the length of beam overlap reduces the linewidth along the ω_τ axis but also reduces signal intensity. A pseudo–time domain filter, where signal prior to the center of the last excitation pulse is excluded from the FID-referenced 2D signal, reduces propagation distortions along the ω_t axis. It is demonstrated that 2DFT rephasing spectra cannot take advantage of an excitation–detection transformation that can eliminate propagation distortions in 2DFT relaxation spectra. Finally, the high optical density experimental 2DFT spectrum of rubidium vapor in argon buffer gas [*J. Phys. Chem. A* **2013**, *117*, 6279–6287] is quantitatively compared, in linewidth, in depth of peak splitting, and in coherent transient peak twisting, to a simulation with optical density higher than that reported.

Keywords

2DFT spectroscopy; Rubidium; propagation distortions

Introduction

Optical two-dimensional Fourier-transform (2DFT) spectroscopy[1–6] is a powerful technique for studying electronic coupling across a wide range of systems, from atomic vapors to biological pigment complexes.

The extra dimension in 2DFT spectroscopy separates homogeneous from inhomogeneous lineshape broadening and highlights coupling between electronic transitions. However, in order to take advantage of this additional information, one must avoid or account for distortions of the signal caused by the absorptive and dispersive nature of the sample.[7–14] Avoidance relegates experimental work to sample optical densities (OD) less than 0.1 where such distortions are typically below 10%,[13] allowing 2DFT spectra to be modeled at the 10% level by ignoring spatial pulse propagation effects at the cost of reduced signal size. In contrast, nonlinear optical signals are typically maximized at optical densities near 0.7,[7] where propagation effects are significant and must be accounted for.[8–16] For linear optics, neglect of propagation distortions corresponds to a restriction that the exponential in Beer's law can be described by a Taylor series expansion that is truncated after the zeroth and first order terms. Because the signal-to-noise ratio of linear absorption spectra are typically optimized at optical densities between 0.3 and 0.7[17,18] where the first-order Taylor series is a poor approximation to the exponential, transmittance spectra are almost always converted to an extinction coefficient using the Beer-Lambert law[19] before modeling. The optical density or absorbance $A = -\log_{10}[I/I_0] = \epsilon CL$ properly accounts for the exponential attenuation of light as it propagates, connecting the macroscopic measurement of the intensity of transmitted light to the microscopic molar decadic extinction coefficient (ϵ), the number density or concentration (C) of chromophores, and the path length (L). The corresponding conversion of 2DFT spectra is not generally so simple, but becomes straightforward in circumstances where 2DFT spectra simplify to changes in transmittance.[3] This paper is about calculating the 2DFT spectra of macroscopic samples even when there is no known procedure for converting the 2DFT spectra to a microscopic nonlinear response. These calculated 2DFT spectra for macroscopic samples are a nonlinear analog of linear transmittance spectra and can be directly compared to experimental 2DFT spectra. Aside from the benefits of maximizing accuracy and signal strength by treating propagation distortions, it is not always possible or practical to control the sample optical density (for example in weakly nonlinear or highly concentrated samples) and the experimental separation of local field and interaction effects (which modify both the linear and nonlinear responses)[7,13,20–26] from propagation effects (in which the underlying linear and nonlinear responses do not change)[7–14] might be accomplished in gases and solutions by independently varying concentration and optical density.[13] Yetzbacher et al. discussed how propagation and detection distortions are influenced by beam crossing angle, beam spot size, signal bandwidth, sample thickness, and sample optical density.[13]

Specifically, the treatment of propagation distortions and their dependence on optical density and beam overlap is the focus of this work.

Ideally, 2DFT spectroscopy is a measurement of the microscopic nonlinear response of a material.[2–4] From this standpoint, propagation effects are 'distortions' of the radiated signal field that change the relationship between the true microscopic nonlinear response and the measured signal field. 2DFT spectra generated by four-wave mixing processes depend on three time intervals, resulting in propagation distortions that are inherently three-dimensional in time or, equivalently, three-dimensional in frequency. Thus, propagation distortions must generally be modeled three-dimensionally, either in the 3D time domain or in the 3D frequency domain.[11,12]

For sufficiently weak excitation fields, propagation distortions in nonlinear optics result from linear reshaping of the excitation pulses and emitted signal field as they propagate through an optically thick medium.[3,11,12,15] For weak, resonant pulses shorter than the polarization decay time of a low optical density medium, each input field propagates almost without distortion, but is trailed by a re-radiated field that is π out of phase with the input field and decays with the polarization decay time (the trailing linear free-induction decay or FID).[27,28] As the optical density increases, multiple absorption–re-radiation cycles increasingly distort the input field and FID. In some work, this effect on the signal has been termed cascaded free-induction decay four-wave mixing[29] because it arises from linear cascading of the input fields; such cascading is fully included in the treatment of propagation distortions here. At optical densities greater than 0.5, these linear propagation distortions are prominent in 2DFT spectra and can even dominate the overall appearance of the lineshape. While it can be advantageous to increase the signal strength by increasing the optical density of the sample, this strategy also strengthens propagation distortions. By including propagation distortions in modeling 2DFT spectra, even highly distorted experimental spectra could be modeled to extract the fundamental dynamics. This ability, which is the nonlinear analog of converting calculated linear extinction coefficients to calculated linear transmittance spectra, would enable the interpretation of 2DFT spectra measured at the optical density where signal is strongest, expanding the range of samples available to 2DFT spectroscopy.

Numerical solutions of the electromagnetic wave equation in one spatial dimension have been used to model spatial propagation, both for intense single pulses[30,31] and for nonlinear signals generated by multiple collinear pulses.[7,9,10,32] Olson et al.[7] used such calculations to distinguish optical density effects

from chromophore interaction effects. Propagation of individual pulses has also been studied using nonlinear finite difference time domain (NL-FDTD) approaches to the solution of Maxwell's equations in three spatial dimensions,[33,34] which treat the boundary conditions as well as intense pulse interactions such as self-focusing. The generality of NL-FDTD methods comes at the computational cost of propagating pulses as an explicit function of both the propagation and transverse dimensions, requiring a 3D spatial grid with sub-wavelength steps ($\lambda/100$ to $\lambda/10$) in addition to a time grid.[33] Pseudospectral time domain methods can increase the maximum allowable spatial step size to as large as $\lambda/2$,[35] reducing the number of spatial grid points necessary for a given propagation length.

The 3DFT method[12] used here to generate and spatially propagate the third-order nonlinear signal is based on an exact, three-dimensional solution of Maxwell's equations and is valid for noncollinear pulses in the weak field limit. This algorithm calculates the complex-valued 3D frequency domain spectrum, $\hat{S}_{3D}$, from which 2DFT spectra at a range of waiting times can be extracted. It successfully reproduces optical density effects on the integrated two-pulse photon echo signal decay rate[11] and beam geometry distortions of relative cross-peak amplitudes in 2DFT infrared spectra.[14] 2DFT spectra calculated using the 3DFT method at waiting times long compared to dipole dephasing dynamics connect to expressions for absolute pump–probe signal size[15,16] and to experimentally-tested expressions for product 2D peak shapes.[3]

The 3DFT algorithm uses the nonlinear impulse response[36,37] (the time-dependent nonlinear polarization excited by three weak, delta-function pulses) as an essential input for the calculation of the signal field radiated by a macroscopic sample. For complicated systems, quantum mechanical time domain propagation of a model system or ensemble of model systems is needed to calculate this response.[38–41] Several approaches to efficiently calculate the response for a single time delay triple have been developed[42,43] and could be incorporated into the algorithm used here. An advantage of the 3DFT algorithm is that the third-order nonlinear response is only calculated once for each point on a 3D grid[11] and does not need to be evaluated at delay-dependent time intervals as in convolution algorithms used to incorporate pulse duration effects.[44–46] While calculating the third-order nonlinear polarization in the time domain usually involves a 3D convolution of the third-order nonlinear susceptibility with the three excitation pulses [requiring $O(N^2)$ operations where N is the total number of points in the 3D grid], this can be accomplished in the frequency domain by simple multiplication following a 3D fast Fourier transform (FFT) of the third-order nonlinear susceptibility [$O(N \log_2 N)$].[47] Alternative methods[48–50] that include interaction with the

pulse fields in repetitive (e.g. phase cycled) calculations of the quantum dynamics have also been used to calculate the nonlinear polarization for finite pulses and generate a computational savings over time domain convolution. These methods optimize the calculation of the polarization for a single time delay triple at one point inside the sample. In contrast, the 3DFT approach is optimized for simultaneous calculation of the entire 3D spectrum, which includes the complete set of 2D spectra (multiplex advantage). Further, propagation distortions can be applied to the 3D signal by a single multiplication in the 3D frequency domain, as opposed to the stepwise pulse propagation and recalculation of the nonlinear polarization for the distorted pulses at each depth within the sample used in the time domain methods.[7,9,10,33–35] Altogether, this results in reduced computation time. The disadvantage is that 3D FFT algorithms typically require more random access memory (RAM) than a 3D convolution, but 3D FFT grids of 1024^3 points that can match available experimental resolution are now possible on personal computers. For grids of even larger size which do not fit in RAM, slower methods allow the 3D Fourier transform to be evaluated in sections.[47]

There are four essential assumptions implicit in the 3D Fourier transform (3DFT) theory and calculations presented here. First, the signal is assumed to be generated by the perturbative third-order nonlinear response of the sample (and it is further assumed that this response is independent of the excitation pulse wave vectors; this excludes signal decay via motion of excited atoms[51] or excitation diffusion,[52] which are slow on femtosecond timescales). Second, it is assumed that the excitation pulses and the radiated signal field all propagate through the sample according to linear optics. [This can be checked for the excitation pulses by measuring their free-induction decay[3,12] (FID) which, unlike absorption measurements, is sensitive to both absorptive and refractive nonlinearity.] Third, the theory assumes that the spectrum and phase of the excitation pulses are uniform across the transverse spatial profile of the pulse (e.g. the beam profile cannot have spatial chirp). Fourth, it is assumed that the excitation beams (a, b, and c) have complete transverse spatial overlap throughout the cell, from the entrance window to the exit window. An approximate treatment of the distortions caused by beams that have no transverse overlap in some portion of the cell is presented below.

The theory excludes nonlinear cascading.[53,54] In nonlinear cascading, a nonlinear signal is generated from one chromophore, propagates to a second chromophore, and acts as an input field in generating an effectively higher-order nonlinear signal from the second chromophore (the prototype nonlinear cascade uses one second-order nonlinear crystal to generate the second harmonic and another for mixing the funda-

mental and second harmonic to generate the third harmonic). The only nonlinear cascade contributing to a third-order signal involves two cascaded second-order nonlinear signals; in an isotropic sample, second-order nonlinear signals can be generated only at interfaces.[55] Second-order nonlinear cascades are ruled out by the experimental geometry, which has no beam overlap at the rear interface. As mentioned above, linear cascading is fully included in the treatment of propagation distortions here.

In rubidium (Rb) atoms, the D_2 ($5^2S_{1/2} \rightarrow 5^2P_{3/2}$) electronic transition is isolated from other transitions and obeys a $\Delta M_J = 0$ selection rule for linearly polarized light, suggesting treatment as an effective two-level system on timescales shorter than that required for hyperfine interactions to manifest [hyperfine splittings for the D_2 transition are less than 6.8 GHz in ^{87}Rb (3.0 GHz in ^{85}Rb)[56]]. Rubidium vapor is an interesting system for studying the validity of a theoretical model for propagation distortions since its optical density can be easily varied over an order of magnitude at constant path length by adjusting the temperature of a rubidium reservoir.[57] Over this range of atomic density, local field effects can be estimated using eq 27 of ref 13; the calculated magnitude of the field experienced by each atom differs from the macroscopic field by less than 0.07%, so that the linear and nonlinear polarizability of non-interacting Rb atoms in Ar buffer gas should dictate the macroscopic linear and nonlinear susceptibility to a similar level of accuracy. The price to be paid is that the linewidth, which is dominated by non-resonant pressure broadening from the argon (Ar) buffer gas, increases with temperature due to the increase in relative intermolecular speed from heating the gas at constant volume. However, this effect is expected to be modest over the temperature range (363–433 K) modeled here: the predicted linewidth at 433 K is approximately 10% greater than that at 363 K.[59] For low partial vapor pressures (~1 mTorr) of alkali metal in noble gases at total pressures of ~1500 Torr, the line broadening in absorption is almost Lorentzian, dominated by pressure broadening from collisions with the noble gas buffer. For the potassium D_1 and D_2 lines, four-wave mixing studies at buffer gas pressures of ~1500 Torr with ~200 fs pulses suggest that the homogeneous optical Bloch model (uncorrelated collisions) underlying a Lorentzian lineshape accounts for the nonlinear response with an 8 ps dephasing timescale.[60] If the line broadening is dominated by isolated binary collisions with a buffer gas, as in ref 57, the Bloch model is expected to be appropriate for Rb vapor. In contrast, correlated collisions typically necessitate models that include frequency memory.[37] In summary, prior work suggests that the Rb D_2 transition dynamics can be characterized by an optical Bloch model, and that as temperature is varied, the changes in its 2DFT spectra should be dominated by

optical density effects.

The homogeneous optical Bloch model includes two phenomenological dipole dephasing processes, each characterized by a single time constant: the population lifetime, T_1, and the pure dephasing time, T_2^*. Assuming that only the excited state population is affected by the population lifetime T_1, the resulting microscopic dipole decay rate is $\Gamma = 1/T_2^* + 1/(2T_1)$.[61] The macroscopic polarization can also decay through inhomogeneous processes, but this is not included here because the Doppler and hyperfine widths are negligible compared to the homogeneous width. Since propagation distortions alter the macroscopic polarization and, consequently, the radiated signal field, the 2DFT spectrum of an optically thick sample will not reflect the chromophore's true microscopic dynamics. Therefore, caution must be exercised when interpreting the Bloch model rates since the 2DFT spectrum of an optically dense sample can be much wider than that of a thin sample,[13] suggesting values of T_2 that are shorter than the true microscopic values. An expression describing the apparent shortening of T_2 in impulsively excited photon echoes for the homogeneous Bloch model is given by eq 3 of ref 11. These propagation distortions depend on T_1.

Based on the known photophysics of the Rb D_2 line, complications that go beyond the two-level Bloch model—but that are still compatible with Bloch model 2DFT spectra—should be expected from at least two sources. First, the 27 ns radiative lifetime of the $^2P_{3/2}$ excited state exceeds the 13 ns interval between pulse sequences at a 76 MHz repetition rate (Ar does not quench Rb D line fluorescence[62–65] and known impurities of N_2, H_2O, and less than 0.0005% O_2 in 99.995% pure industrial grade Ar suggest a maximum quenching rate[64,66] of 6×10^6 s^{-1}). This means that approximately one-third of the 2D signal may derive from prior pulse sequences. Second, collisions can transfer the Rb atoms out of the optically excited M_J states (the measured cross sections[67,68] predict a ~20 ps timescale for loss of rotational alignment). For all-parallel polarized pulses, the nonlinear response (hence 2DFT spectra) can be decomposed into a sum of a population response (which should decay with the population lifetime of ~27 ns) and an alignment response (which should decay with the alignment lifetime of ~20 ps).[69–71] Both alignment and population nonlinear responses have the same total dephasing time T_2[72] which arises primarily from Ar collisions causing either a change in phase or a change in alignment, with a much smaller contribution from the radiative lifetime. As a result, the 2DFT spectra at the nominal experimental waiting time of $T = 200$ fs are expected to be the weighted sum of three parts: (1) a population 2DFT spectrum with $T = 200$ fs, population lifetime $T_1 = 27$ ns, and $T_2 \approx 12$ ps; (2) a population 2DFT spectrum with $T > 13$ ns from

prior pulses; and (3) an alignment 2DFT spectrum with $T = 200$ fs, alignment lifetime $T_1 \approx 20$ ps, and $T_2 \approx 12$ ps.[76] In addition, hyperfine relaxation is slow so that parallel polarized optical pumping[77] can generate a steady-state modification of the response.[56] Unlike the two effects mentioned above, hyperfine pumping effects increase the order of the nonlinear response beyond third order; however, in steady-state, it can be regarded as modifying the third-order nonlinear response discussed above. In the absence of propagation distortions, the three Bloch model 2DFT spectra expected to contribute to the total 2DFT spectrum are identical for nominal waiting times T greater than the pulse duration.

This paper follows a paper detailing experimental work by Li et al.[57] on propagation distortions in 2DFT spectra of rubidium vapor. We present a theoretical and computational treatment of novel distortions observed in the experimental 2DFT spectra. However, quantitative modeling of the experimental lineshapes was not attempted for two reasons. First, the asymmetry between ω_τ and ω_t linewidths in the low-OD experimental spectra is not recovered by the Bloch model or the Kubo stochastic model[11] (in the slow-, intermediate-, and fast-modulation limits). Second, the linewidth and peak OD of experimental linear absorption spectra are inconsistent with predicted linear absorption spectra at each experimental Rb reservoir temperature under the assumption that the Rb vapor density is given by the vapor pressure of Rb at the experimentally measured reservoir temperature. In addition, the linewidth and peak OD implied by the experimental 2DFT spectra do not agree with either the experimental or the predicted linear absorption spectra. Repetitive excitation might contribute to the latter discrepancies through steady-state modifications on the effective linear and nonlinear responses. In the face of these disagreements, the linewidth was set constant for all simulated 2DFT spectra in order to focus on qualitative OD-dependent features present in the experimental 2DFT spectra. The above disagreements will be addressed further in the Discussion section.

Theory

Propagation Distortions

A complete mathematical framework for describing propagation and detection distortions on 2DFT spectra in the 3D frequency domain has been developed.[12–14] This discussion highlights the essentials necessary

to understand the distortions that are the focus of this work and presents an improved approximation for the incoherent limit of the propagation function. First, in order to discuss the propagation of pulses in a sample, we will define the time domain optical electric field of the excitation pulses,

$$\mathbf{E}(\mathbf{r},t) = \frac{1}{2\pi}\int_{-\infty}^{\infty} \hat{\mathbf{E}}(\mathbf{r},\omega)\ \exp\left(-\mathrm{i}\omega t\right) \mathrm{d}\omega \tag{1}$$

where $\mathbf{r}$ is spatial position, t is time, and ω is the angular frequency. $\hat{\mathbf{E}}(\mathbf{r},\omega)$ is the frequency domain complex-valued electric field,

$$\hat{\mathbf{E}}(\mathbf{r},\omega) = \frac{1}{(2\pi)^3}\iiint \hat{\boldsymbol{\mathcal{E}}}(\hat{\mathbf{k}}(\omega),\omega)\ \exp\left[\mathrm{i}\hat{\mathbf{k}}(\omega)\cdot\mathbf{r}\right] \mathrm{d}^3\hat{\mathbf{k}} \tag{2}$$

where $\hat{\boldsymbol{\mathcal{E}}}(\hat{\mathbf{k}}(\omega),\omega)$ is a "wave" which, when integrated over $\hat{\mathbf{k}}$, is equal to the frequency domain complex-valued electric field at the center of the sample entrance plane ($\mathbf{r} = 0$). The spatial variation of the "wave" simply factors out into $\exp[\mathrm{i}\hat{\mathbf{k}}(\omega)\cdot\mathbf{r}]$, where $\hat{\mathbf{k}}(\omega)$ is the complex-valued wave vector, which incorporates attenuation of the electric field when propagating through absorbing media. Representing the pulses as waves is convenient in that it mathematically separates propagation effects from the input pulse fields, allowing the propagation effects to be collected and dealt with separately. Throughout this paper, vectors and matrices are in bold face type while complex-valued quantities are marked with a circumflex (or "hat"). For normal incidence, the wave vector is $\hat{\mathbf{k}}(\omega) = \mathbf{e}_z\,\hat{n}(\omega)\,\omega/c$ where $\mathbf{e}_z$ is the unit vector normal to the window–sample interface and c is the speed of light in vacuum. $\hat{n}(\omega) = n(\omega) + \mathrm{i}\kappa(\omega) = \sqrt{\hat{\epsilon}(\omega)/\epsilon_0}$ is the complex-valued refractive index, $\hat{\epsilon}(\omega)$ is the complex-valued permittivity (dielectric constant), and ϵ_0 is the permittivity of vacuum (MKS units). Attenuation of the field is contained in the imaginary part of the wave vector, $\mathrm{Im}[\|\hat{\mathbf{k}}(\omega)\|] = \kappa(\omega)\,\omega/c$, which is related to the napierian (i.e. base e) field attenuation coefficient,[78] $\alpha(\omega) = \kappa(\omega)\,\omega/c = A(\omega)\ln(10)/2L$, where $A(\omega)$ is the decadic absorbance[78] (optical density) and L is the sample length normal to the window–sample interfaces.[13] α and A are linked by $T = I/I_0 = e^{-2\alpha L} = 10^{-A}$ where T is the transmittance of the sample. The usage of α here for the *field* attenuation coefficient is not to be confused with the *intensity* attenuation coefficient (napierian absorption coefficient), which is also denoted by α in some cases.[78]

For a weak absorber (i.e. $\kappa^2 \ll n^2$), the wave vector can be expressed in a more general form that is

valid for oblique incidence as well as normal incidence:

$$\hat{\mathbf{k}}(\omega) \approx (\omega/c)\,[n(\omega)\,\mathbf{u} + \mathrm{i}\kappa(\omega)\,\mathbf{e}_z/(\mathbf{u}\cdot\mathbf{e}_z)] \tag{3}$$

where $\mathbf{u}$ is the unit vector along the direction of propagation (which can be calculated using the ordinary real-valued Snell's Law [see eqs A6 and A7 of ref 12]). The real and imaginary parts of a complex-valued wave vector are normal to planes of constant phase and amplitude respectively and, therefore, point in different directions (see Figure 18-6 of ref 79) except for normally incident light (i.e. $\mathbf{u} = \mathbf{e}_z$). The factor of $1/(\mathbf{u}\cdot\mathbf{e}_z)$ modifies κ to account for the additional path length when beams are not at normal incidence to the window–sample interface. This is necessary because $\mathrm{Im}[\hat{\mathbf{k}}(\omega)]$ is parallel to the window–sample interface normal, not the propagation vector. Propagation from the sample cell entrance at $\mathbf{r}$ to the sample cell exit at $\mathbf{r} + \mathbf{u}\,\ell$ multiplies the wave by $\exp[\mathrm{i}\,\omega(n + \mathrm{i}\kappa)\ell/c]$, where $\ell = L/(\mathbf{u}\cdot\mathbf{e}_z)$ is the path length through the sample for a beam propagating along $\mathbf{u}$.

Given the following three additional assumptions, the propagation matrix for the 3D frequency domain signal field[12] can be simplified to a scalar:[13] (1) well-collimated beams, (2) transverse electric (TE) polarized beams, and (3) an isotropic nonlinear susceptibility. Accordingly, vector and matrix notation are dropped for the fields and susceptibility. We further assume that the sample and windows have the same linear optical properties so that no linear reflections are generated by the window–sample interfaces (see Appendix C of ref 12). 3D inverse Fourier transformation of the time domain third-order nonlinear response (eq B3 of ref 12) yields the 3D frequency domain nonlinear susceptibility, $\hat{\chi}^{(3)}$, which is multiplied by the three excitation waves (a, b, and c) to form the nonlinear polarization wave inside the sample, $\hat{\mathcal{P}}^{(3)}$. Further multiplication by the propagation function, $\Pi^{(3)}_{\mathrm{exit}}$, gives the radiated signal wave referenced to the sample exit, $\hat{\mathcal{E}}_t$; multiplication by the directional filter function, $\Phi^{(3)}$, isolates the particular phase-matched signal field that is selected for interference detection with respect to the detection wave, $\hat{\mathcal{E}}_d$. The detection wave may represent an actual reference pulse propagating through the sample in the direction of the signal, but may also represent an artificial wave that incorporates both the actual reference (which may be routed around the sample) and measured differences between the actual reference and a chosen ideal reference (for example, the reference-tracer phase difference of refs 80, 1, and 3 or the amplitude distortion from propagating through an absorptive sample treated in ref 13). The result is the transmitted

3D frequency domain signal,

$$\begin{aligned}\hat{S}_{3D} &\approx \hat{\mathcal{E}}_t\, \hat{\mathcal{E}}_d^*\, \Phi^{(3)} \\ &\approx \frac{i\omega_t}{2\epsilon_0 c} \left[\Pi_{\text{exit}}^{(3)}\, \hat{\mathcal{P}}^{(3)}\right] \hat{\mathcal{E}}_d^*\, \Phi^{(3)} \\ &\approx \frac{i\omega_t}{2\epsilon_0 c} \left[\Pi_{\text{exit}}^{(3)} \left(\hat{\chi}^{(3)}\, \hat{\mathcal{E}}_a\, \hat{\mathcal{E}}_b\, \hat{\mathcal{E}}_c\right)\right] \hat{\mathcal{E}}_d^*\, \Phi^{(3)}\end{aligned} \tag{4}$$

where $\hat{\mathcal{E}}_{a,b,c,d}$ represent the excitation (a, b, c) and detection (d) pulse waves and $\omega_t = \omega_c + \omega_b - \omega_a$ is the frequency of the transmitted signal wave. In eq 4, the arguments of the waves follow the signs of the frequencies in ω_t: $\hat{\mathcal{E}}_a(-\omega_a)$, $\hat{\mathcal{E}}_b(\omega_b)$, $\hat{\mathcal{E}}_c(\omega_c)$, and $\hat{\mathcal{E}}_d^*(\omega_t)$.[12] (For waves, changing the sign of the frequency argument has the same effect as complex conjugation.) The mathematical form of the directional filter is given by eq 56 of ref 12. For this experiment, $\Phi^{(3)}$ is over 50 times wider than the experimental 2DFT spectrum and has no significant effect beyond selecting only two conjugate octants of the 3D frequency domain signal, which physically reflects detection of signal from only one phase-matched direction. Within the rotating-wave approximation, the directional filter is implemented here by calculating the nonlinear response using only diagrams that give a phase-matched signal for the detected beam. Given the three assumptions listed above, the propagation function takes the form (eq 9 of ref 13)

$$\begin{aligned}&\Pi_{\text{exit}}^{(3)}(\hat{\mathbf{k}}_a^0, \hat{\mathbf{k}}_b^0, \hat{\mathbf{k}}_c^0, L) = \\ &\qquad \frac{\omega_t}{\left(\hat{\mathbf{k}}_s^0 \cdot \mathbf{e}_z\right) c} \frac{\exp\left[i\left(\Delta\hat{\mathbf{k}}^0 \cdot \mathbf{e}_z\right) L\right] - 1}{i\left(\Delta\hat{\mathbf{k}}^0 \cdot \mathbf{e}_z\right)} \exp\left[i\left(\hat{\mathbf{k}}_s^0 \cdot \mathbf{e}_z\right) L\right]\end{aligned} \tag{5}$$

where $\hat{\mathbf{k}}_{a,b,c,s}^0$ are the complex-valued frequency-dependent central wave vectors of the excitation pulses (a, b, c) and the signal (s) inside the sample, ω_t is the frequency of the transmitted signal wave, and $\Delta\hat{\mathbf{k}}^0 = \hat{\mathbf{k}}_p^0 - \hat{\mathbf{k}}_s^0$ is the complex-valued 3D phase mismatch between the nonlinear polarization and signal waves, with central wave vectors $\hat{\mathbf{k}}_p^0$ and $\hat{\mathbf{k}}_s^0$ respectively. A superscript "0" indicates use of the central wave vector approximation. The true wave vector distribution of each beam includes the angular spread of wave vectors needed for the focused beam diameter. In the central wave vector approximation, the propagation function is evaluated at each beam's central wave vector. This approximation requires well collimated beams and is implicit in the use of a directional filter, which accounts for the wave vector distribution.[12] In the limit of $(\Delta\hat{\mathbf{k}}^0 \cdot \mathbf{e}_z)L \ll 1$ and small beam crossing angles, the propagation function

approaches the normal incidence result, $\Pi^{(3)}_{\text{exit}} \approx [L/\hat{n}(\omega_t)] \exp[\mathrm{i}(\hat{\mathbf{k}}^0_s \cdot \mathbf{e}_z)L]$. The proportionality to L physically represents perfectly phase-matched growth of signal over the length of the sample and the exponential represents linear propagation. For a sample much thinner than a wavelength of light, the normal-incidence propagation function further simplifies to $\Pi^{(3)}_{\text{exit}} \approx L/\hat{n}(\omega_t)$.

In the rectangular BOXCARS geometry, three parallel excitation beams are arranged such that each intersects the corner of a rectangle. The beams are focused into the sample, producing a signal beam which intersects the fourth corner of the rectangle (see Figure 1 of ref 13) if all four frequencies are the same. The nonlinear polarization wave has central wave vector

$$\hat{\mathbf{k}}^0_p(\omega_t) = \hat{\mathbf{k}}^0_a(-\omega_a) + \hat{\mathbf{k}}^0_b(\omega_b) + \hat{\mathbf{k}}^0_c(\omega_c) \tag{6}$$

determined by the three excitation pulse wave vectors.[12] $\hat{\mathbf{k}}^0_p$ is a function of all three input frequencies; this dependence is suppressed here for compactness. The imaginary part of $\hat{\mathbf{k}}^0_a(-\omega_a)$ correctly incorporates attenuation of forward propagating pulse a [$-\hat{\mathbf{k}}^0_a(\omega_a) = \hat{\mathbf{k}}^0_a(-\omega_a)^*$ attenuates backward propagation and would incorrectly amplify forward propagation]. Maxwell's equations require[12] that the signal wave vector obeys the boundary condition

$$\hat{\mathbf{k}}^0_s \cdot \mathbf{e}_{x,y} = \hat{\mathbf{k}}^0_p \cdot \mathbf{e}_{x,y} \tag{7}$$

with

$$\hat{\mathbf{k}}^0_\gamma(\omega) \cdot \hat{\mathbf{k}}^0_\gamma(\omega) = \left(\omega^2/c^2\right) \hat{n}^2(\omega) \tag{8}$$

for all four beams ($\gamma = a, b, c, s$). $\hat{\mathbf{k}}^0_s$ is also a function of all three input frequencies. Equation 8, which applies to linearly propagating electromagnetic waves, need not hold for the nonlinear polarization wave vector: for unequal input frequencies, the real parts of the signal and polarization wave vectors can differ in both magnitude and direction (see Figure 1 of ref 13); for equal input frequencies, the imaginary part of the polarization wave vector is 3 times greater than the imaginary part of the signal wave vector, reflecting attenuation of all three excitation beams.

The 3D nonlinear susceptibility, $\hat{\chi}^{(3)}$, is multiplied by the propagation function (eq 5), the excitation pulse waves ($\hat{\mathcal{E}}_{a,b,c}$), the detection pulse wave ($\hat{\mathcal{E}}^*_d$), and the directional filter to produce the distorted 3D

frequency domain signal,

$$\begin{aligned}\hat{S}_{3D}(\omega_a, -\omega_b, -\omega_c) \approx \Pi^{(3)}_{\text{exit}}(\hat{\mathbf{k}}^0_a, \hat{\mathbf{k}}^0_b, \hat{\mathbf{k}}^0_c, L) \\ \cdot \frac{i\omega_t}{2\varepsilon_0 c}\hat{\chi}^{(3)}(-\omega_a, \omega_b, \omega_c) \\ \cdot \hat{\mathcal{E}}_a(-\omega_a)\,\hat{\mathcal{E}}_b(\omega_b)\,\hat{\mathcal{E}}_c(\omega_c) \\ \cdot \hat{\mathcal{E}}^*_d(\hat{\mathbf{k}}_d, \omega_t)\,\Phi^{(3)}(\omega_a, -\omega_b, -\omega_c)\end{aligned} \tag{9}$$

The distorted 3D frequency domain signal is triple Fourier transformed into the 3D time domain. Given that $t_a \leq 0$, $t_b \leq 0$, and $t_c = 0$ are the experimentally controlled arrival times of pulses a, b, and c, respectively, we define the time intervals $T \equiv \min(|t_a|, |t_b|)$ and $\tau \equiv t_b - t_a$. The time domain 2D signal, $S_{2D}(t, \tau; T)$, at fixed waiting time T is extracted from the 3D time domain signal according to

$$\begin{aligned}S_{2D}(t, \tau; T) = S_{3D}(t + \tau + T, t + T, t)\,\theta(\tau) \\ + S_{3D}(t + T, t - \tau + T, t)\,\theta(-\tau)\end{aligned} \tag{10}$$

where $\theta(\tau)$ is the Heaviside unit step function. The time domain 2D signal from eq 10 is inverse Fourier transformed (along τ and t) back to the frequency domain to produce the complex-valued 2DFT spectrum,

$$\begin{aligned}\hat{S}_{2D}(\omega_t, \omega_\tau; T) = \frac{1}{\omega_t\, e(\omega_t)} \int_{-\infty}^{\infty}\int_{-\infty}^{\infty} S_{2D}(t, \tau; T) \\ \cdot \exp(i\omega_\tau \tau)\ \exp(i\omega_t t)\, d\tau dt\end{aligned} \tag{11}$$

where $e(\omega_t)$ is the detection pulse field envelope, which represents the frequency envelope of the detection field, and ω_t and ω_τ are conjugate to t and τ, respectively. Division by ω_t removes the radiative distortion that is introduced by the factor of ω_t on the second line of eq 9. The form of the detection envelope in eq 11 depends on the detection geometry utilized and will be specified for each representation discussed below.

To calculate the complex-valued *rephasing* 2D spectrum, only the positive-τ part of the time domain

2D signal is inverse Fourier transformed:

$$R\hat{S}_{2\mathrm{D}}(\omega_t, \omega_\tau; T) = \frac{1}{\omega_t\, e(\omega_t)} \iint_{-\infty}^{\infty} S_{2\mathrm{D}}(t, \tau; T)\, \theta(\tau) \cdot \exp\left(\mathrm{i}\omega_\tau \tau\right)\, \exp\left(\mathrm{i}\omega_t t\right) \mathrm{d}\tau \mathrm{d}t \tag{12}$$

Multiplication by the Heaviside unit step function (see p. 61 of ref 81), $\theta(\tau)$, in eq 12 selects the positive-τ rephasing pulse ordering, where pulse a comes before pulse b, by multiplying $S_{2\mathrm{D}}(t, \tau < 0, T)$ by 0, $S_{2\mathrm{D}}(t, \tau = 0, T)$ by $1/2$, and $S_{2\mathrm{D}}(t, \tau > 0, T)$ by 1; this is equivalent to neglecting the second term in eq 10. The factor of $1/2$ at $\tau = 0$ is essential to prevent baseline offset in a discrete Fourier transform.[81] In this paper, all rephasing spectra will be indicated by "R". Most of the 2DFT spectra depicted here are calculated according to eq 12 to allow for direct comparison to the experimental work by Li et al.[57]

Since it is instructive to compare distorted and undistorted 2DFT spectra, we define the *ideal* (undistorted) 2DFT spectrum, $\hat{S}_{2\mathrm{D}}^{\mathrm{ideal}}$, which is calculated using eq 11 where the propagation function is taken to be

$$\Pi_{\mathrm{exit}}^{\mathrm{ideal}}(L) = \frac{\omega_t L}{\left(\mathbf{k}_{sv}^0 \cdot \mathbf{e}_z\right) c} = \frac{L}{\left(\mathbf{u}_s \cdot \mathbf{e}_z\right)} \tag{13}$$

where $\mathbf{k}_{sv}^0$ is the real-valued signal central wave vector in vacuum and $\mathbf{u}_s$ is the unit propagation vector of the signal beam. This "ideal" propagation function is valid for samples with no absorptive or refractive effects (i.e. $\hat{n} = 1$) and neglects the effect of phase mismatch, which even in vacuum only vanishes for collinear beams or zero sample length.[13] Vacuum phase mismatch is negligible in the experiment of Li et al.,[57] making eq 13 a good approximation for this work. Since all of the representations of the 2DFT spectrum discussed in the next section are equivalent in the limit of optically thin samples, the ideal 2DFT spectrum requires no indication of representation and is directly comparable to distorted spectra in any representation.

Representations of the 2DFT Spectrum

Experimental Distinctions

In order to address the form of the detection field, the experimental detection geometry must be discussed. In 2DFT spectroscopy, the amplitude and phase of the signal field is retrieved by interference with a detection field. Since the 3D signal (eq 4) is dependent on the detection field, it must be well characterized to extract the signal field from the spectral interferograms. The detection field is used to establish the zero of spectral phase, which also specifies the time axis for the signal field relative to the excitation pulses. The three representations of 2DFT spectra used here (attenuated, FID-referenced, and time-referenced) have been discussed in more detail elsewhere.[13,14]

Experimentally, either the tracer beam ("ref II"[57]) or the reference beam ("ref I"[57]) can be used for interferometric detection of the signal field. The amplitude and phase of the detection field directly influence the amplitude and phase of the 2DFT spectrum extracted from experimental interferograms and can be used to approximately remove certain propagation distortions. The cost of changing representations is that the 2DFT spectrum may no longer be an accurate representation of the signal field that exits the sample. In the BOXCARS geometry, the tracer beam occupies one corner of the rectangle formed on the focusing lens by it and the three excitation beams and copropagates with the signal through the sample and on to the detector.[3,80] Since the tracer copropagates with the signal, it accrues the same linear absorptive and dispersive distortions as the signal through the sample and common path optics. However, the tracer can influence or be influenced by nonlinear interactions with the excitation pulses. The reference beam bypasses the sample, but later rejoins and copropagates with the signal beam to the detector. In bypassing the sample, the reference beam avoids all sample-induced distortions. However, this also means that it encounters a different set of optics and travels a different length, taking on phase and attenuation that is not common to the signal. The tracer can be used without the excitation pulses to characterize the time origin and phase of the reference beam relative to the excitation pulses at the sample.[3,80] For a more detailed description of the experimental geometry, see Figure 2 of ref 57.

Attenuated

In the attenuated representation of the 2DFT spectrum, the tracer beam, which propagates along the same path as the signal through the sample, serves directly as the detection field.[13] In this case, assuming a weakly absorbing sample, the complex-valued wave vector of the detection beam is given by

$$\hat{\mathbf{k}}_d^0(\omega_t) = \frac{\omega_t}{c}\left[n(\omega_t)\,\mathbf{u}_d + \mathrm{i}\frac{\kappa(\omega_t)}{(\mathbf{u}_d \cdot \mathbf{e}_z)}\mathbf{e}_z\right] \tag{14}$$

where $\mathbf{u}_d$ is the unit propagation vector of the detection beam, which—for the BOXCARS geometry—is collinear with the central wave vector of the tracer beam. In the square BOXCARS geometry, with the detection beam aligned such that $\mathbf{u}_d = \mathbf{u}_c + \mathbf{u}_b - \mathbf{u}_a$, Maxwell's equations guarantee that the components of the wave vector parallel to the window–sample interface are the same for $\hat{\mathbf{k}}_s^0$ and $\hat{\mathbf{k}}_d^0$ (hence $\hat{\mathbf{k}}_s^0 = \hat{\mathbf{k}}_d^0$ and $\mathbf{u}_s = \mathbf{u}_d$ when all four frequencies are the same). Thus, all effects for the parallel components of $\hat{\mathbf{k}}_s^0$ and $\hat{\mathbf{k}}_d^0$ automatically cancel (recall that the imaginary part of a wave vector attenuates the wave along an axis normal to the window–sample interface). At the sample exit plane ($z = L$), the detection wave has the form

$$\hat{\mathcal{E}}_d(\omega_t) = \hat{\mathcal{E}}_d^0(\omega_t)\,\exp\left\{\mathrm{i}\left[\hat{\mathbf{k}}_d^0(\omega_t)\cdot\mathbf{e}_z\right]L\right\} \tag{15}$$

where $\hat{\mathcal{E}}_d^0(\omega_t)$ is the detection wave at the sample entrance ($\mathbf{r} = 0$) for zero delay. Since the tracer and signal take the same path through the sample, the tracer beam experiences approximately the same attenuation and dispersion as the signal [$\hat{\mathbf{k}}_d^0(\omega_t) \approx \hat{\mathbf{k}}_s^0(-\omega_a, \omega_b, \omega_c)$]. This approximation is valid within a 3D signal frequency-bandwidth inversely proportional to the excitation beam crossing angles, is good when the signal beam is well-collimated, and is an equality for collinear excitation beams at normal incidence. Replacing $\hat{\mathbf{k}}_d^0$ with $\hat{\mathbf{k}}_s^0$ yields

$$\hat{\mathcal{E}}_d(\omega_t) \approx \hat{\mathcal{E}}_d^0(\omega_t)\,\exp\left\{\mathrm{i}\left[\hat{\mathbf{k}}_s^0(-\omega_a, \omega_b, \omega_c)\cdot\mathbf{e}_z\right]L\right\} \tag{16}$$

for the detection wave at the sample exit plane. For small angles of incidence or when $\kappa^2 \ll n^2$, this further simplifies to

$$\hat{\mathcal{E}}_d(\omega_t) \approx \hat{\mathcal{E}}_d^0(\omega_t)\, \exp\left\{\frac{\omega_t}{c}\left[\mathrm{i}\,(\mathbf{u}_d \cdot \mathbf{e}_z)\, n(\omega_t) - \frac{\kappa(\omega_t)}{(\mathbf{u}_d \cdot \mathbf{e}_z)}\right] L\right\} \tag{17}$$

To calculate the attenuated rephasing 2DFT spectrum $[R\hat{S}_{2\mathrm{D}}^{-}(\omega_t, \omega_\tau; T)]$ from eq 12, eq 16 is used as the detection wave in eq 9, taking $e(\omega_t) = 1$ for the detection pulse field envelope. Using $e(\omega_t) = 1$ ignores the effect of the detection field's spectrum on the amplitude of the signal field recovered from spectral interferograms. As a result, the real part of the attenuated 2DFT spectrum, when integrated over ω_τ, becomes equal to the spectrally resolved pump-probe signal when directional filtering distortions are negligible.[13]

The substitution of $\hat{\mathbf{k}}_s^0$ for $\hat{\mathbf{k}}_d^0$ in the exponential term of eq 16 is useful in that it results in cancellation of the imaginary part of the final exponential term in the propagation function (eq 5) when both equations are combined to form the 3D signal (eq 4). In contrast, the real parts have the same sign and, consequently, add. Physically, this signifies that while there is cancellation of phase evolution between the signal and tracer (i.e. no relative phase), the attenuation of the signal and detection fields is additive, resulting in stronger absorptive distortions in the 2DFT spectrum. The spectra measured using the "reference through the sample" in the work by Li et al.[57] are fundamentally attenuated rephasing 2D spectra. However, the spectra depicted in Figures 4 and 5 of ref 57 have been processed with a time domain filter and are no longer in the $R\hat{S}_{2\mathrm{D}}^{-}$ representation. The effect of this filter is discussed in the section "Pseudo–Time Domain Filtering" below.

FID-referenced

While the tracer can be used as the detection field for interferometric detection, attenuation and dispersion of the tracer in an absorptive sample can introduce distortions into the measured 2DFT spectrum. In addition, if the tracer falls within the time window of the sample nonlinear response, it has the potential to interact with the sample in such a way as to alter the radiated signal field or be altered by nonlinear interaction with the sample. To avoid such attenuation and nonlinear interaction, the tracer can be used to characterize the reference and then can be blocked during the experiment, using the reference beam

directly for interference detection.[80] In this case, the tracer must be used to characterize the phase accrued by the signal in traversing the sample. Under the same approximations as eq 16, this detection geometry results in the detection wave

$$\hat{\mathcal{E}}_d(\omega_t) \approx \hat{\mathcal{E}}_d^0(\omega_t)\, \exp\left\{\mathrm{i}\,\mathrm{Re}\left[\hat{\mathbf{k}}_s^0(-\omega_a, \omega_b, \omega_c)\cdot\mathbf{e}_z\right] L\right\} \tag{18}$$

which can be used in eq 9 to calculate the FID-referenced rephasing 2DFT spectrum, $R\hat{S}_{2\mathrm{D}}^0(\omega_t, \omega_\tau; T)$, from eq 12 given that $e(\omega_t) = |\hat{\mathcal{E}}_d^0(\omega_t)|$. For small angles of incidence or when $\kappa^2 \ll n^2$, this further simplifies to

$$\hat{\mathcal{E}}_d(\omega_t) \approx \hat{\mathcal{E}}_d^0(\omega_t)\, \exp\left[\mathrm{i}\omega_t\, (\mathbf{u}_d\cdot\mathbf{e}_z)\, n(\omega_t)\, L/c\right] \tag{19}$$

The FID-referenced representation differs from the attenuated representation only in that the attenuation of the detection field is removed. Both $\hat{S}_{2\mathrm{D}}^-$ and $\hat{S}_{2\mathrm{D}}^0$ have the FID phase removed, resulting in a physically meaningful separation of the 2DFT spectrum into absorptive (real) and dispersive (imaginary) parts.[13] However, this comes at the expense of losing a causal time origin such that the 2DFT spectrum of an optically thick sample contains signal that appears to arrive before pulse c.

Fundamentally, the spectra denoted by "reference around the sample" in the work by Li et al.,[57] such as those in Figure 3 of ref 57, are measurements of the FID-referenced rephasing 2D spectrum. However, since only the amplitude (absolute value) of the experimental spectra is shown in ref 57, the phase evolution contained in the exponential term in eq 18 is hidden.

An approximation to $R\hat{S}_{2\mathrm{D}}^0$ can be calculated by transforming the attenuated 2DFT spectrum $R\hat{S}_{2\mathrm{D}}^-$ (where the tracer is used as the detection wave) to account for detection wave attenuation. This procedure results in

$$\begin{aligned} R\hat{S}_{2\mathrm{D}}^0(\omega_t, \omega_\tau; T) &\approx R\hat{S}_{2\mathrm{D}}^-(\omega_t, \omega_\tau; T) \\ &\quad\cdot \left|\hat{\mathcal{E}}_d^0(\omega_t)\right| \exp\left\{\mathrm{Im}\left[\hat{\mathbf{k}}_d^0(\omega_t)\cdot\mathbf{e}_z\right] L\right\} \\ &\approx R\hat{S}_{2\mathrm{D}}^-(\omega_t, \omega_\tau; T) \\ &\quad\cdot \left|\hat{\mathcal{E}}_d^0(\omega_t)\right| \exp\left[\omega_t \kappa(\omega_t)\ell/c\right] \end{aligned} \tag{20}$$

where $\ell = L/(\mathbf{u}_d\cdot\mathbf{e}_z)$ is the path length through the sample cell for the detection beam and

$R\hat{S}^{-}_{2D}(\omega_t, \omega_\tau; T)$ is the attenuated rephasing 2D spectrum as described in the previous section. This is an approximation insofar as it substitutes the attenuation of the signal along the complex-valued central wave vector of the detection beam in the sample, $\hat{\mathbf{k}}^0_d(\omega_t)$, for the true signal attenuation in $\hat{\mathbf{k}}^0_s$ given by eqs 6–8, which involves a range of wave vectors that are dependent on all three excitation frequencies.

Time-referenced

Neglecting the effects of signal field propagation, the time-referenced 2D spectrum is a direct reflection of the underlying bulk nonlinear polarization of the sample. This representation is calculated using

$$\hat{\mathcal{E}}^t_d(\omega_t) = \hat{\mathcal{E}}^0_d(\omega_t)\, \exp\left\{\mathrm{i}\left[\mathbf{k}^0_{sv}(-\omega_a, \omega_b, \omega_c)\cdot \mathbf{e}_z\right] L\right\} \tag{21}$$

as the form of the detection wave where $\mathbf{k}^0_{sv}$ is the signal central wave vector in vacuum. The time-referenced rephasing 2D spectrum, $R\hat{S}^t_{2D}(\omega_t, \omega_\tau; T)$, is calculated from eq 12 by using eq 21 as the detection wave in eq 9 given that $e(\omega_t) = |\hat{\mathcal{E}}^0_d(\omega_t)|$.

$R\hat{S}^t_{2D}$ can be calculated in an approximate way starting from $R\hat{S}^0_{2D}$:

$$\begin{aligned} R\hat{S}^t_{2D}(\omega_t, \omega_\tau; T) \approx\ & R\hat{S}^0_{2D}(\omega_t, \omega_\tau; T) \\ & \cdot \exp\left\{\mathrm{i}\,\mathrm{Re}\left[\hat{\mathbf{k}}^0_d(\omega_t) - \mathbf{k}^0_{dv}(\omega_t)\right]\cdot \mathbf{e}_z L\right\} \end{aligned} \tag{22}$$

where $\mathbf{k}^0_{dv}$ is the real-valued central wave vector of the detection beam in vacuum and $\hat{\mathbf{k}}^0_d$ is the complex-valued central wave vector of the detection beam in the sample. The exponential in eq 22 approximates the FID phase due to the sample by using the central wave vector of the detection beam, which depends on only one frequency, instead of the wave vector of the signal, which depends on all three excitation frequencies. This approximation, just as with eqs 16 and 18, is valid for a well-collimated signal beam and becomes exact for collinear excitation beams at normal incidence. Time-referenced 2DFT spectra have delays from the refractive index of the sample because they are time-referenced to when pulse c would emerge from the sample if it propagated through vacuum. The time-referenced and FID-referenced representations only differ in the phase of the detection field and, consequently, the phase of the 2DFT spectrum. Therefore, the absolute value 2DFT spectra in these representations are identical: $|R\hat{S}^t_{2D}| = |R\hat{S}^0_{2D}|$. However, the

phase differences between time-referenced and FID-referenced 2DFT spectra cause them to be affected differently by time domain filters.

Transformation of 2DFT Spectra

As demonstrated by Yetzbacher et al.,[13] it is possible to transform calculated and experimental 2DFT spectra in such a way as to approximately remove the distortions caused by attenuation of excitation and signal fields. The result is the excitation–detection transformed 2D spectrum,

$$\begin{aligned}\hat{S}^{++}_{\mathrm{2D}}(\omega_t, \omega_\tau; T) &= \frac{2\,\mathrm{Im}\left[\hat{\mathbf{k}}^0_\tau(\omega_\tau)\cdot\mathbf{e}_z\right] L}{1-\exp\left\{-2\,\mathrm{Im}\left[\hat{\mathbf{k}}^0_\tau(\omega_\tau)\cdot\mathbf{e}_z\right] L\right\}} \\ &\quad\cdot \exp\left\{\mathrm{Im}\left[\hat{\mathbf{k}}^0_d(\omega_t)\cdot\mathbf{e}_z\right] L\right\} \\ &\quad\cdot \hat{S}^0_{\mathrm{2D}}(\omega_t, \omega_\tau; T) \\ &\approx \frac{2\omega_\tau \kappa(\omega_\tau)\ell/c}{1-\exp\left[-2\omega_\tau\kappa(\omega_\tau)\ell/c\right]} \\ &\quad\cdot \exp\left[\omega_t\kappa(\omega_t)\ell/c\right] \\ &\quad\cdot \hat{S}^0_{\mathrm{2D}}(\omega_t, \omega_\tau; T)\end{aligned} \tag{23}$$

where $\hat{\mathbf{k}}_\tau$ is the wave vector of the initial excitation pulse ($\hat{\mathbf{k}}_a$ or $\hat{\mathbf{k}}_b$). The second expression in eq 23 arises from approximating $\hat{\mathbf{k}}^0(\omega)$ using the approximation of eq 3, which is valid as long as either $\kappa^2 \ll n^2$ or the angle of incidence is small (i.e. $\mathbf{u} \approx \mathbf{e}_z$). In the rectangular BOXCARS geometry, 2α and 2β are defined as the external crossing angles (in vacuum or air) between beams a and c (as well as b and d) and beams a and b (as well as c and d), respectively. In this geometry, the path length through the sample is given by $\ell = L/\gamma$ where $\gamma = \mathbf{u}\cdot\mathbf{e}_z = (1-\sin^2\alpha-\sin^2\beta)^{1/2}$ and is equal for all beams (a, b, c, and d), permitting use of the same ℓ in eq 23 for propagation along both the excitation dimension (ω_τ) and the detection dimension (ω_t). Equation 23 neglects vacuum phase mismatch so that $\mathbf{u}_s \approx \mathbf{u}_d$. A reformulation of eq 23

in terms of the absorbance of the sample is given by

$$\begin{aligned}\hat{S}_{\mathrm{2D}}^{++}(\omega_t,\omega_\tau;T) \approx & \frac{A(\omega_\tau)\ln(10)/\gamma}{1-10^{-A(\omega_\tau)/\gamma}} \\ & \cdot 10^{A(\omega_t)/(2\gamma)} \\ & \cdot \hat{S}_{\mathrm{2D}}^{0}(\omega_t,\omega_\tau;T)\end{aligned} \tag{24}$$

where $A(\omega)$ is the decadic absorbance at normal incidence. In the limit of no coherence (i.e. $\omega_t = \omega_c$ and $\omega_a = \omega_b$), eqs 23 and 24 recover the ideal 2DFT spectrum, $\hat{S}_{\mathrm{2D}}^{\mathrm{ideal}}$.

Analytic Bloch Model 2DFT Spectrum

An analytic form is known for the impulsive correlation (waiting time $T = 0$) and relaxation ($T > 0$) 2DFT peak shapes of the homogeneous optical Bloch model:[82]

$$\begin{aligned}\hat{S}_{\mathrm{2D}}^{\mathrm{ideal}}(\omega_t,\omega_\tau,T) \propto & \\ & a(-\omega_\tau)a(\omega_t) - \mathrm{i}a(-\omega_\tau)d(\omega_t) \\ & + \frac{1}{2}\delta(T)\big[a(-\omega_\tau)a(\omega_t) + d(-\omega_\tau)d(\omega_t) \\ & \quad - \mathrm{i}a(-\omega_\tau)d(\omega_t) + \mathrm{i}d(-\omega_\tau)a(\omega_t)\big] \\ & + a(\omega_\tau)a(-\omega_t) + \mathrm{i}a(\omega_\tau)d(-\omega_t) \\ & + \frac{1}{2}\delta(T)\big[a(\omega_\tau)a(-\omega_t) + d(\omega_\tau)d(-\omega_t) \\ & \quad + \mathrm{i}a(\omega_\tau)d(-\omega_t) - \mathrm{i}d(\omega_\tau)a(-\omega_t)\big]\end{aligned} \tag{25}$$

where

$$a(\omega) = \frac{\Gamma^2}{\left(\omega_{eg}-\omega\right)^2+\Gamma^2} \tag{26}$$

and

$$d(\omega) = \frac{\left(\omega_{eg}-\omega\right)\Gamma}{\left(\omega_{eg}-\omega\right)^2+\Gamma^2} \tag{27}$$

are Lorentzian absorptive and dispersive lineshape functions, respectively, with central transition frequency ω_{eg} and width defined by Γ, the Bloch microscopic dipole decay rate. Γ is equal to the half-width

half-maximum (HWHM) of a Lorentzian absorptive lineshape and is the inverse of the dipole decay (or dephasing) time: $\Gamma = 1/T_2$. Equations 26 and 27 differ from eq 18 of Gallagher Faeder and Jonas [82] in that they have been peak normalized through multiplication by Γ. Here, "impulsive" is used to signify that pulses a, b, and c have δ-function time domain profiles. Although the analytic 2DFT peak shape in eq 25 is a sum of product lineshapes that have no correlation between the two dimensions ω_τ and ω_t, the 2DFT peak shape does exhibit correlation at $T = 0$. This analytic form is useful in that it can be compared to numerical calculations to confirm that they accurately reproduce the spectral lineshape in the Bloch limit, which serves as a basis for understanding more complex coherent phenomena that occur as a function of T with the introduction of propagation distortions.

The absolute value of the impulsive *rephasing* 2DFT peak shape was experimentally measured by Li et al..[57] For the homogeneous optical Bloch model, the one dimensional absolute value lineshape is $(a^2 + d^2)^{1/2} = a^{1/2}$, and the absolute value rephasing 2DFT peak shape for positive T is given by

$$\begin{aligned} \left| R\hat{S}_{2\mathrm{D}}^{\mathrm{ideal}}(\omega_t, \omega_\tau, T) \right| &\propto \sqrt{a(\omega_\tau)\, a(\omega_t)} \\ &\propto \left[\frac{\Gamma^2}{\left(\omega_{eg} + \omega_\tau\right)^2 + \Gamma^2} \cdot \frac{\Gamma^2}{\left(\omega_{eg} - \omega_t\right)^2 + \Gamma^2} \right]^{1/2} \end{aligned} \tag{28}$$

with FWHM $= 2\sqrt{3}\,\Gamma$ in both the ω_t and ω_τ dimensions (a $\sqrt{3}$ increase in linewidth for both dimensions compared to the real 2DFT relaxation spectrum). As will be shown below, the distortions of 2D peak shapes in absolute value rephasing spectra are more complicated than those for 2D peak shapes in relaxation spectra.

Incoherent 2D Propagation Function

The incoherent limit of the propagation function depends on only two frequencies and serves as an exact baseline for identifying coherent transient propagation effects. Multiplying the propagation function in eq 5 by the complex conjugate of the propagation factor for the detection field, $\exp[\mathrm{i}\,\mathrm{Re}(\hat{\mathbf{k}}_s^0 \cdot \mathbf{e}_z)L]^*$, as

indicated by eqs 4 and 18, yields

$$\begin{aligned}\Pi^{(3)}_{\text{exit}}(\hat{\mathbf{k}}^0_a, \hat{\mathbf{k}}^0_b, \hat{\mathbf{k}}^0_c, L)\ &\exp\left[-\mathrm{i}\,\mathrm{Re}\left(\hat{\mathbf{k}}^0_s \cdot \mathbf{e}_z\right) L\right] \\ &= \frac{\omega_t}{\left(\hat{\mathbf{k}}^0_s \cdot \mathbf{e}_z\right) c} \frac{\exp\left[\mathrm{i}\left(\Delta\hat{\mathbf{k}}^0 \cdot \mathbf{e}_z\right) L\right] - 1}{\mathrm{i}\left(\Delta\hat{\mathbf{k}}^0 \cdot \mathbf{e}_z\right)} \exp\left[-\,\mathrm{Im}\left(\hat{\mathbf{k}}^0_s \cdot \mathbf{e}_z\right) L\right]\end{aligned} \tag{29}$$

This form of the propagation function is specific to FID-referenced 2DFT spectra. Incorporating eqs 44 and 47 of ref 12 for $\hat{\mathbf{k}}^0_s$ and $\Delta\hat{\mathbf{k}}^0$ plus the three assumptions listed below, the 3D propagation function in eq 29 can be simplified to a 2D function of ω_τ and ω_t. First, the signal is assumed to be generated in the incoherent limit where $\omega_a = \omega_b \equiv \omega_\tau$ and $\omega_c = \omega_t$. Second, it is assumed that the sample is weakly absorbing ($\kappa^2 \ll n^2$) such that the approximate form of the wave vector in eq 3 is valid. Third, $\hat{n}_{zs}$ and $\hat{n}_z$ are approximated as equal, which assumes that $|4(\omega_\tau/\omega_t)(1 - \omega_\tau/\omega_t)\sin^2\beta| \ll 1$ (i.e. the limit of small fractional bandwidth $\Delta\omega/\omega$ and small angles of incidence). Under these conditions, eq 29 simplifies to

$$\begin{aligned}\Pi^0_{\text{2D}}(\omega_t, \omega_\tau, L) = &\\ &\frac{1}{\hat{n}_{zs}(\omega_t)} \frac{\exp\left[(-2\omega_\tau \kappa_z(\omega_\tau)/c)\, L\right] - 1}{(-2\omega_\tau \kappa_z(\omega_\tau)/c)} \\ &\cdot \exp\left[-\,\mathrm{Im}\left(\omega_t \hat{n}_z(\omega_t)/c\right) L\right]\end{aligned} \tag{30}$$

The factor of $1/\hat{n}_{zs}(\omega)$ arises from the boundary conditions for Maxwell's equations at the sample–window interfaces.[12] Substituting $\kappa_z(\omega) = \kappa(\omega)\ell/L$ as implied by eqs 41 and 42 of ref 12, we arrive at the incoherent propagation function appropriate for FID-referenced 2DFT spectra,

$$\begin{aligned}\Pi^0_{\text{2D}}(\omega_t, \omega_\tau, L) = &\\ &\frac{L}{\hat{n}_{zs}(\omega_t)} \frac{\exp\left[-2\omega_\tau \kappa(\omega_\tau)\ell/c\right] - 1}{-2\omega_\tau \kappa(\omega_\tau)\ell/c} \\ &\cdot \exp\left[-\omega_t \kappa(\omega_t)\ell/c\right]\end{aligned} \tag{31}$$

All factors besides $L/\hat{n}_{zs}(\omega)$ represent absorptive propagation distortions and tend to unity as the sample length tends to zero.[83] $\hat{n}_{zs}(\omega)$ physically represents the effective complex-valued refractive index for the z-component of propagation of the signal field and is applicable to pulses with arbitrary angles of incidence α and β (see eq 41 of ref 12). The imaginary component of the complex-valued refractive index can be

expressed in the convenient form

$$\kappa(\omega) = \frac{c}{\omega_{eg}} \alpha_{\max}\, a(\omega) \tag{32}$$

where $\alpha_{\max} = \alpha(\omega_{eg})$ is the peak attenuation coefficient. $a(\omega)$ is the absorptive lineshape function which, for the homogeneous Bloch model, is given by eq 26. The propagation function in eq 31 is almost the inverse of the excitation–detection transformation in eq 23, but differs by a factor of $L/\hat{n}_{zs}(\omega_t)$ which can contribute a phase shift from the sample–window interfaces when κ is not negligible compared to n. In the incoherent limit, the FID-referenced 2DFT spectrum becomes

$$\begin{aligned} \hat{S}^0_{\mathrm{2D}}(\omega_t, \omega_\tau; T) \approx\ & \hat{S}^{\mathrm{ideal}}_{\mathrm{2D}}(\omega_t, \omega_\tau, T) \\ & \cdot \frac{\Pi^0_{\mathrm{2D}}(\omega_t, \omega_\tau, L)}{\Pi^{\mathrm{ideal}}_{\mathrm{exit}}(L)} \end{aligned} \tag{33}$$

where $\Pi^{\mathrm{ideal}}_{\mathrm{exit}}(L) = \ell$ in the rectangular BOXCARS geometry.

To calculate the attenuated 2DFT spectrum starting from eq 25, the factor of $\exp\{-\mathrm{Im}[\hat{\mathbf{k}}^0_s(-\omega_a, \omega_b, \omega_c) \cdot \mathbf{e}_z]L\} \approx \exp[-\omega_t \kappa(\omega_t)\ell/c]$ in eq 16 is incorporated into the propagation function, resulting in a form that is specific to the attenuated 2DFT spectrum:

$$\begin{aligned} &\Pi^-_{\mathrm{2D}}(\omega_t, \omega_\tau, L) = \\ &\quad \frac{L}{\hat{n}_{zs}(\omega_t)} \frac{\exp\left[-2\omega_\tau \kappa(\omega_\tau)\ell/c\right] - 1}{-2\omega_\tau \kappa(\omega_\tau)\ell/c} \\ &\quad \cdot \exp\left[-2\omega_t \kappa(\omega_t)\ell/c\right] \end{aligned} \tag{34}$$

The modified propagation function in eq 34, when applied to the analytic 2DFT signal calculated using eq 25, yields

$$\begin{aligned} \hat{S}^-_{\mathrm{2D}}(\omega_t, \omega_\tau; T) \approx\ & \hat{S}^{\mathrm{ideal}}_{\mathrm{2D}}(\omega_t, \omega_\tau, T) \\ & \cdot \frac{\Pi^-_{\mathrm{2D}}(\omega_t, \omega_\tau, L)}{\Pi^{\mathrm{ideal}}_{\mathrm{exit}}(L)} \end{aligned} \tag{35}$$

The analytic expressions in eqs 33 and 35 are useful for comparison to numerical calculations of $\hat{S}^0_{\mathrm{2D}}$ and $\hat{S}^-_{\mathrm{2D}}$ respectively, which should match the analytic results for the limit in which both $T \gg T_2$ and $2T_1 \gg T_2$. While likely more stringent than necessary, these two conditions are sufficient to guarantee

that $\hat{S}_{2D}(\omega_t, \omega_\tau; T) \propto \int_{-\infty}^{\infty} \hat{S}_{2D}(\omega_t, \omega_\tau; T)\, dT$. By the projection–slice theorem,[81,84] this proportionality to the waiting-time–averaged 2DFT spectrum guarantees that a 2DFT spectrum has $\omega_T = |\omega_a - \omega_b| = 0$, implying $\omega_a = \omega_b$ and, consequently, $\omega_c = \omega_t$. In this circumstance, the analytic form of the propagation function in eqs 31 and 34 must be valid for any relaxation model. These two conditions imply both that the waiting time must be long enough that all dynamics in T are finished ($T \gg T_2$) and that the lifetime is sufficiently long that incoherent population relaxation completely dominates the time-averaged 2DFT spectrum ($2T_1 \gg T_2$).

Computation

Methods

The program used to calculate 2DFT spectra was written in Fortran 95/2003 and compiled using the Intel Visual Fortran Compiler Professional 11.1.070.[85] This program was executed on a computer with a 3.2 GHz Core i7 processor and 24 GB of random access memory (RAM) running 64-bit Windows 7 Professional. The calculations utilized a grid size of 1024^3, where each grid point is a complex, double-precision number, requiring a total of ~17 GB of RAM and ~8 min of execution time. Complex, double-precision Fourier transforms were accomplished using the DFFT3B, DFFT3F, DFFT2B, and DFFT2F subroutines of the International Mathematics and Statistics Library (IMSL) Fortran Numerical Library version 6.0.[86]

Approximations

While the effects of finite-bandwidth excitation pulses are easily handled in the 3DFT approach, excitation pulses have been approximated as delta-function pulses. This is a good approximation for this study since the bandwidth of the excitation pulses ($\Delta\omega_{FWHM}/2\pi c \approx 126\ \mathrm{cm}^{-1}$) is 250 times greater than the linewidth of the D_2 transition ($\Delta\omega_{FWHM}/2\pi c \approx 0.5\ \mathrm{cm}^{-1}$). The effects of this approximation are even smaller than the effects of neglecting the directional filtering distortions discussed previously. Over the frequency range shown, the maximum fractional error in the linear susceptibility from the rotating-wave approximation[28] is less than 10^{-4}, so rotating-wave errors in the 2DFT spectrum are expected to be neg-

ligible. The expressions for testing the validity of the 3DFT approach developed by Yetzbacher et al.[13] indicate that the conditions of the experiment by Li et al.[57] satisfy the essential assumptions implicit in the 3DFT theory with one exception: significant error arises from the assumption that excitation beams have complete transverse overlap, as will be discussed below.

Estimation of Convergence

To characterize the error associated with using a discrete and finite-size grid in these calculations, four types of convergence tests were performed. First, the effect of using a grid with a finite time range was explored by comparing two $\hat{S}_{2D}^{-}$ absolute value 2DFT spectra calculated using different grid sizes (512^3 vs 1024^3) with identical time domain sampling intervals. The two compared spectra have the same frequency range because they have the same time step size, but have frequency step sizes differing by a factor of 2 due to their different time ranges. This type of comparison is used to expose problems associated with finite frequency resolution and, equivalently, a finite time range. The percent difference between 2DFT spectra calculated on the two grid sizes is determined by subtracting the absolute value spectra at common (ω_τ, ω_t) grid points and then dividing by the global maximum of the 2DFT spectrum. For all calculations reported here, the difference between these absolute value spectra at any point is less than 1.5% of the maximum. This error appears as ringing along the 2D diagonal.

Second, the effect of using a grid of discrete time points was tested by comparing two $\hat{S}_{2D}^{-}$ absolute value 2DFT spectra, one on a 1024^3 grid and the other on a 512^3 grid with double the time step size. Since both spectra have the same time range, they have an identical frequency step size. However, the spectra have different time step sizes, resulting in different frequency ranges. This comparison is meant to uncover errors related to the finite frequency range and, equivalently, the finite time resolution of the calculation. In order to compare the two spectra, the spectrum calculated using a 1024^3 grid is cropped to the same frequency range as the spectrum calculated on a 512^3 grid. For all calculations reported here, the difference between these absolute value spectra at any point is less than 4.5% of the maximum. Consistent with eq 25, this error arises from the imaginary (refractive) peak shape at the edge of the grid as discussed in Comparison to Analytic Theory.

Third, the deviation caused by using a long excited state population lifetime ($T_1 = 30$ ns in most

simulations) compared to the time range of the 3DFT grid (~0.87 ns in most simulations) has been characterized. To adequately resolve sharp features in the core of the 2D peak shape, which are dominated by fast dephasing dynamics ($\lesssim$20 ps for the D_2 transition of Rb under the conditions of interest here[57]) and propagation distortions, a grid step size of 850 fs was used in most of the simulations. To quantify the effect of time domain truncation of slow excited state population relation dynamics, a 2DFT spectrum simulated directly at $T_1 = 30$ ns was compared to a 2DFT spectrum that was point-by-point linearly extrapolated, as a function of $1/T_1$, from $T_1 = 120$ ps and $T_1 = 240$ ps to $T_1 = 30$ ns. In both cases, the spectra were absolute value time-referenced rephasing 2DFT spectra ($|R\hat{S}^t_{2D}|$) with $OD_{max} = 1.14$; grid time step, 850 fs; grid size, 1024^3; dephasing rate, $\Gamma/2\pi c = 0.265\ cm^{-1}$; center frequency, $\omega_{eg}/2\pi c = 12816.7\ cm^{-1}$; mixing time, $T = 850$ fs; sample thickness, $L = 500\ \mu m$; and crossing angles, $\alpha = \beta = 4.84°$. The maximum absolute deviation between the 2DFT spectrum extrapolated to $T_1 = 30$ ns from untruncated time domain data and that calculated directly at $T_1 = 30$ ns is less than 0.5% of the maximum.

Fourth, the effect of using a longer waiting time ($T = 850$ fs in most simulations) than that of the experiment ($T = 200$ fs) was determined. Since the nonlinear polarization is calculated on a 3D grid of evenly spaced time/frequency points, choice of waiting times is restricted to integer multiples of the grid time step size. To quantify the difference between simulations at the experimental waiting time versus a longer waiting time, 2DFT spectra simulated at $T = 200$ fs and a grid time step of 200 fs were compared to 2DFT spectra simulated at $T = 850$ fs and a grid time step of 850 fs. In both cases, the spectra were absolute value time-referenced rephasing 2DFT spectra ($|R\hat{S}^t_{2D}|$) with $OD_{max} = 1.14$; grid size, 1024^3; dephasing rate, $\Gamma/2\pi c = 0.265\ cm^{-1}$; excited state lifetime, $T_1 = 30$ ns; center frequency, $\omega_{eg}/2\pi c = 12816.7\ cm^{-1}$; sample thickness, $L = 500\ \mu m$; and crossing angles, $\alpha = \beta = 4.84°$. The maximum absolute deviation between these 2DFT spectra is less than 3.6%. This difference is largely the result of the two 2DFT spectra having dissimilar frequency ranges and is consequently isolated to the wings of the 2D peak shape. Deviations within the core of the peak are less than 1.5% of the maximum.

Comparison to Analytic Theory

The convergence tests above quantify precision deficiencies of the second most converged calculation. Comparisons to analytic theory are used to assess the absolute accuracy of the most converged calcula-

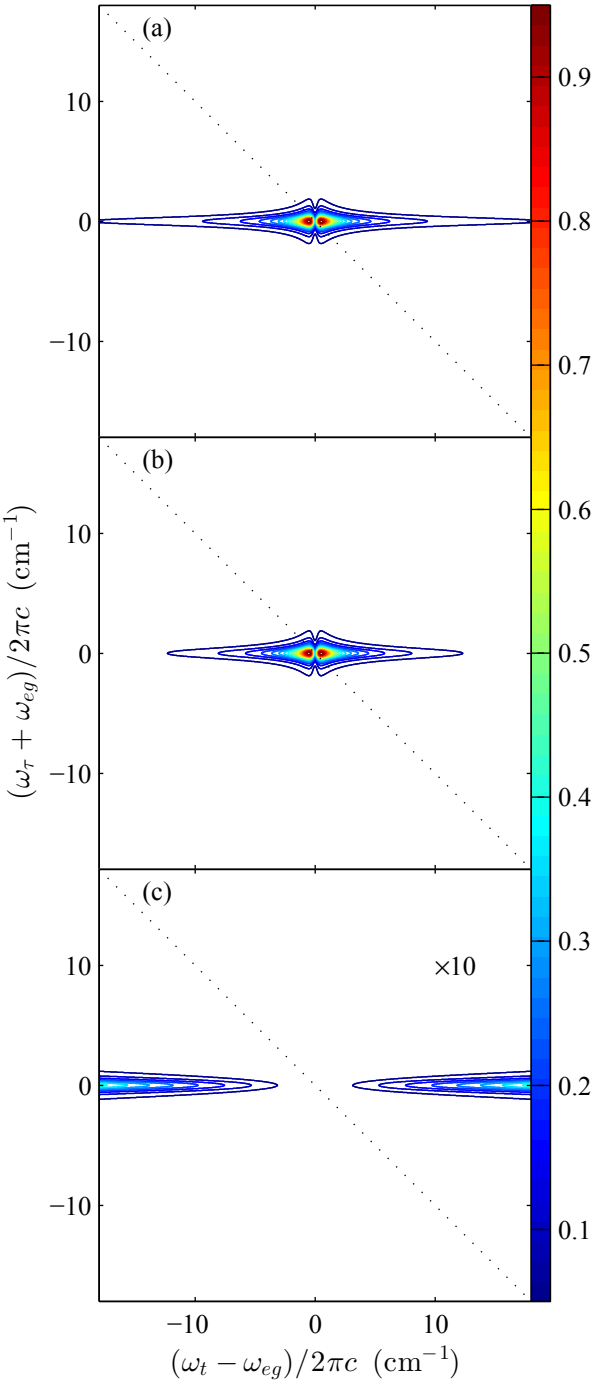

Figure 1: Absolute value 2DFT relaxation spectra for Bloch model in the $\hat{S}^{-}_{2D}$ representation (a) calculated using the analytic form of the 2DFT spectrum from eq 25 in eq 35 and (b) calculated numerically using eq 16 in eqs 9–11. The scaled difference between spectra in (a) and (b), calculated according to $|(a) - (b)| \times 10$, is presented in (c). Peak optical density, $\mathrm{OD}_{\mathrm{max}} = 1$; grid time step, 850 fs; grid size, 1024^3; dephasing rate, $\Gamma/2\pi c = 0.265\ \mathrm{cm}^{-1}$; excite state lifetime, $T_1 = 30$ ns; center frequency, $\omega_{eg}/2\pi c = 12816.7\ \mathrm{cm}^{-1}$; waiting time, $T = 100.3$ ps; sample thickness, $L = 500\ \mu$m; and crossing angles, $\alpha = \beta = 4.84°$. There are 19 contours, evenly spaced every 5% from 5% to 95%, in (a) and (b) but only 8 contours, spaced every 0.5%, in (c). The dotted line indicates the diagonal: $\omega_t = -\omega_\tau$. For ease of comparison, the limits for both frequency axes correspond exactly to those of Figure 4 in ref 57.

tions in specific limits. The analytic form of the impulsive Bloch 2DFT spectrum in eq 25 can be used to calculate spectra for comparison to spectra calculated using the 3DFT method with OD = 0. This comparison can serve as a test that the 3DFT calculation accurately reproduces the peak shape of the Bloch 2DFT spectrum when propagation distortions are absent.

Analytic 2DFT spectra that include propagation distortions have also been derived above for checking numerical results. The 2D form of the propagation function presented in eq 34 is valid in the limit that $T \gg T_2$ and $2T_1 \gg T_2$. The 2D propagation function (eq 34) can be multiplied by the analytic impulsive Bloch 2DFT spectrum (eq 25) to produce an analytic $\hat{S}^{-}_{2D}$ spectrum (eq 35) for comparison to $\hat{S}^{-}_{2D}$ spectra calculated numerically using the 3DFT method. The results of this comparison are shown in Figure 1 for $OD_{max} = 1$. In contrast to the single peak of the ideal absolute value 2DFT relaxation spectrum calculated from eq 25, both spectra have a vertical gash from absorption at $\omega_t = \omega_{eg}$, which generates peak splitting. The primary difference between the analytic $\hat{S}^{-}_{2D}$ spectrum in Figure 1a and the numerical $\hat{S}^{-}_{2D}$ spectrum in Figure 1b is that the wings of the lineshape in the ω_t dimension of the numerical spectrum are lower than those of the analytic spectrum. This effect becomes more pronounced with increasing $|\omega_t - \omega_{eg}|$ and reaches a value of 4.2% at the edge of the plot.

Given that the majority of the spectral amplitude in the wings of a Bloch lineshape is in the imaginary part, which contains information regarding refractive effects that are dominated by short-time dynamics, most of the disagreement between the analytic and numerical spectra in Figure 1 is confined to the imaginary part of the spectrum. The real parts of the numerical and analytic $\hat{S}^{-}_{2D}$ spectra differ by less than 0.7% for $OD_{max} = 1$.

The differences in Figure 1 are an artifact of the Fourier-transform since they occur near the edges of the 2DFT grid where the signal amplitudes must be equal due to the cyclic nature of the conjugate axis in the FFT algorithm (see Figure 11.4 of ref 81). Since the FFT of a real-valued time domain signal obeys $\hat{S}(-\omega) = \hat{S}^{*}(\omega)$, the imaginary part of the frequency domain spectrum has odd symmetry and, therefore, must tend towards zero at the edge of the frequency domain grid. The magnitude of this artifact will be negligible in the limit that the frequency range of the 3DFT grid is much greater than the linewidth of the spectrum.

Motivated by the disagreement between experiment and simulation with regard to the magnitude of absorptive distortions at a given optical density, a comparison between 2D propagation function "spectra"

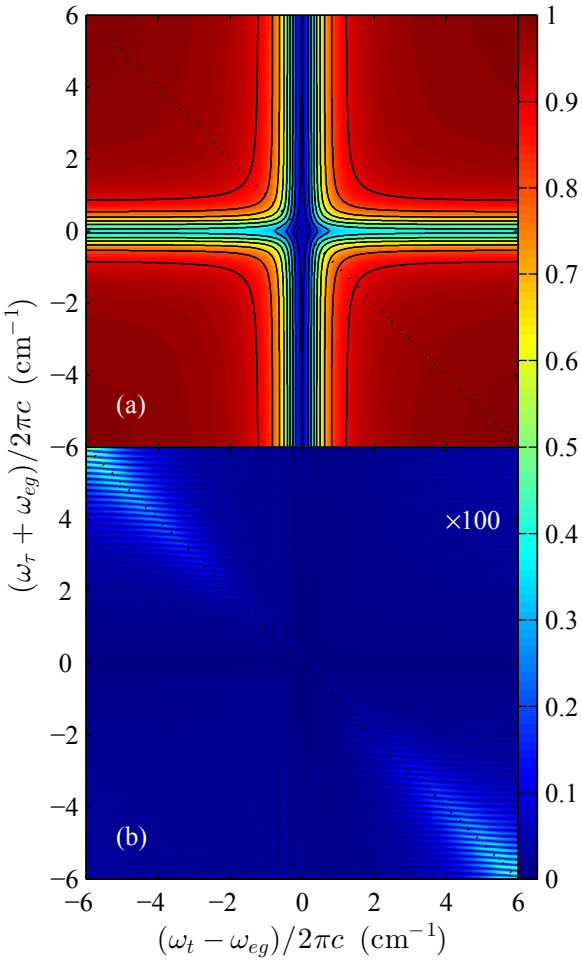

Figure 2: The 2D propagation function, $|\Pi^{-}_{2D}(\omega_t, \omega_\tau, L)/\ell|$, for the $\hat{S}^{-}_{2D}$ representation. Panel (a) is calculated with the Bloch model from the ratio of absolute value numerical 2DFT spectra given by eq 36. The absolute value of the difference between the numerical propagation function in (a) and the absolute value of the analytic form given by eq 34 is multiplied by 100 in panel (b). Peak optical density, $\mathrm{OD}_{\mathrm{max}} = 1$; grid time step, 850 fs; grid size, 1024^3; dephasing rate, $\Gamma/2\pi c = 0.265\ \mathrm{cm}^{-1}$; dephasing time, $T_2\ (= 1/\Gamma) = 20$ ps; excited state lifetime, $T_1 = 30$ ns; center frequency, $\omega_{eg}/2\pi c = 12816.7\ \mathrm{cm}^{-1}$; waiting time, $T = 100.3$ ps; sample thickness, $L = 500$ μm; and crossing angles, $\alpha = \beta = 4.84°$. There are 100 color levels, meaning that each color represents a 1% range. There are 9 contours in panel (a), evenly spaced every 10% from 10% to 90%. The dotted line indicates the diagonal: $\omega_t = -\omega_\tau$.

calculated by the 3DFT method and those calculated from a simple analytic expression was undertaken to verify, at least in the incoherent limit, that the 3DFT method correctly accounts for the magnitude of signal attenuation. When $2T_1 \gg T_2$ and $T \gg T_2$, signal generation is restricted to cases where $\omega_a = \omega_b$. In this limit, the ratio $\hat{S}^{-}_{2D}/\hat{S}^{\text{ideal}}_{2D}$ approaches the incoherent propagation function:

$$\lim_{\omega_a \to \omega_b} \frac{\hat{S}^{-}_{2D}(\omega_t, \omega_\tau; T)}{\hat{S}^{\text{ideal}}_{2D}(\omega_t, \omega_\tau; T)} = \frac{\Pi^{-}_{2D}(\omega_t, \omega_\tau, L)}{\Pi^{\text{ideal}}_{\text{exit}}(L)} = \frac{\Pi^{-}_{2D}(\omega_t, \omega_\tau, L)}{\ell} \tag{36}$$

In the incoherent limit, the ratio of complex valued 2DFT spectra in eq 36 becomes equal to the ratio of absolute value 2DFT spectra if the phase introduced by $\hat{n}_{zs}$ can be neglected over the entire frequency range in eq 34. Figure 2a shows the 2D version of the propagation function calculated using the ratio of absolute value numerical 2DFT spectra indicated by the left-hand side of eq 36, where $\hat{S}^{\text{ideal}}_{2D}(\omega_t, \omega_\tau; T)$ is calculated as $\hat{S}^{0}_{2D}(\omega_t, \omega_\tau; T)$ with $\text{OD}_{\text{max}} = 0$ (see eq 13). A plot of the ratio of absolute value analytic propagation functions indicated by the right-hand side of eq 36 is almost visually identical to Figure 2a. Figure 2b depicts the difference (multiplied by a factor of 100) between the numerical 2D propagation function (ratio of absolute value 2DFT spectra indicated by the left-hand side of eq 36) and the analytic 2D propagation function in the incoherent limit, Π^{-}_{2D}/ℓ (ratio of absolute value 2D propagation functions indicated by the right-hand side of eq 36), where Π^{-}_{2D} is calculated using eq 34. Given that $T_1 = 1500T_2$, a converged accuracy limit for this comparison is likely set by the use of $T \approx 5T_2$ in Figure 2a.

For frequencies where the distorted 2DFT signal ($|\hat{S}^{-}_{2D}|$) is above the 5% level, the difference shown in Figure 2b never exceeds 0.07%. At the extremes of the diagonal, a ringing artifact of the discrete Fourier-transform is visible with an amplitude of up to ~0.6%. Ringing, which is more pronounced along the diagonal than the antidiagonal in Figure 2c, only appears in the numerical 2D propagation function (eq 36) and only at frequencies far from resonance, where the artifact is non-negligible compared to the amplitude of the signal. The difference has a local minimum along each dimension at $|\omega| = \omega_{eg}$. The approximate incoherent propagation function in eq 60 of ref 12 generates larger, numerically significant, disagreements of 0.3% for signals above the 5% level; the improved agreement here depends upon the better approximation of eq 31 for the incoherent propagation function.

Equation 36 can simplified for the case $-\omega_\tau = \omega_t = \omega_{eg}$ given that $\hat{n}_{zs} = \hat{n}_z$ under these conditions.

This yields the attenuation at peak center for $\hat{S}^{-}_{2D}$ 2DFT spectra in the incoherent limit,

$$\frac{\left|\Pi^{-}_{2D}(\omega_{eg},\omega_{eg},L)\right|}{\left|\Pi^{\text{ideal}}_{\text{exit}}(L)\right|} = \frac{\gamma}{\left|\hat{n}_z(\omega_{eg})\right|}\,\frac{1-10^{-A(\omega_{eg})/\gamma}}{\ln(10)\,A(\omega_{eg})/\gamma}\,10^{-A(\omega_{eg})/\gamma} \tag{37}$$

where $A(\omega_{eg}) = \text{OD}_{\text{max}}$ is the decadic absorbance (optical density) of the sample at normal incidence and $\gamma = (1 - \sin^2\alpha - \sin^2\beta)^{1/2}$ accounts for the additional path length at oblique incidence (see eq 24). When at least one of $-\omega_\tau = \omega_t$ (i.e. $\omega_a = \omega_b = \omega_c$) or $\beta = 0$ is true, using $\hat{n}_z$ in place of $\hat{n}_{zs}$ is exact, as is the case in eq 37. The single-point attenuation in eq 37 can be readily calculated by hand to check a more complicated 3DFT code. For an optical density of 1, the ratio $|\hat{S}^{-}_{2D}|/|\hat{S}^{\text{ideal}}_{2D}| = |\Pi^{-}_{2D}|/|\Pi^{\text{ideal}}_{\text{exit}}|$ at the peak center in Figure 2b (0.03828 ± 0.00003) is only 0.11% higher than the attenuation predicted by eq 37 using the same parameters (0.03824), a discrepancy attributable to ringing. Inverting the numerical ratio of $|\Pi^{-}_{2D}|/|\Pi^{\text{ideal}}_{\text{exit}}| = 0.03828$ using eq 37 with $\hat{n}_z(\omega_{eg}) = 0.9929 + 0.0003\text{i}$ and $\gamma = 0.9929$ yields $\text{OD}_{\text{max}} = 0.9997 \pm 0.0003$ (which agrees within error with $\text{OD}_{\text{max}} = 1$). The attenuation factors appearing in eqs 36 and 37 have been experimentally tested to 10% accuracy in frequency-integrated pump–probe experiments for peak optical densities of up to 1 (see the absorption coefficient–dependent terms in eqs 24 and 26 of ref 15).

Calculations by the 3DFT method quantitatively reproduce the Bloch lineshape of an undistorted 2DFT spectrum.[13] The comparison in Figure 1 shows that the 3DFT method reproduces propagation distorted 2DFT spectra in the incoherent limit (waiting time T much greater than the dephasing time T_2), with the largest numerical errors in the far wings due to the finite grid. The comparison in Figure 2 between the incoherent 2D propagation function calculated by the 3DFT program (where grid errors largely cancel due to the ratio in eq 36) and that calculated using the analytic expression in eq 34 demonstrates quantitative agreement, matching in signal attenuation over the entire range of relevant frequencies at a peak optical density of 1. This agreement with experimentally tested expressions confirms that the 3DFT program properly accounts for the magnitude of propagation distortions given the sample's optical density. This rules out many possible errors in the program's code as causes of disagreement between experiment and simulation. This comparison does not ensure the accuracy of coherent propagation effects at waiting times that are not long compared to the total dephasing time (i.e. $T \not\gg T_2$).

Results

Line broadening coefficients reported from frequency domain experiments[58,87–91] at Ar buffer gas pressures from 0 atm to 100 atm indicate that at the buffer gas and Rb vapor pressures deduced from the experimental temperatures,[57] line broadening is dominated by non-resonant, binary Rb–buffer collisions. This, along with the experimental observation of a Lorentzian absorption lineshape[57] and Bloch model simulations of prior time-resolved experiments[31,60] on alkali metal vapors, motivated use of an optical Bloch model that describes the lineshape of the Rb D_2 transition with a single, homogeneous broadening timescale, T_2. This timescale enters the Bloch model as the dipole decay rate (or total dephasing rate) $\Gamma = 1/T_2$ in the exponential decay of dipole oscillations $\mu(t) = \mu_0 \sin(\omega_{eg} t) \exp(-\Gamma t)$. On the other hand, in studies of the potassium vapor at atomic densities 3 to 5 orders of magnitude higher than the present work, a stochastic model is used to treat frequency memory in resonance broadened lineshapes.[92–94] A total dephasing time $T_2 = 20$ ps, corresponding to a dipole decay rate of $\Gamma = 50$ rad/ns and a Lorentzian absorption lineshape[91] with FWHM $= \Gamma/(\pi c) = 0.53$ cm^{-1}, was used for the calculations presented here. All plots of 2DFT spectra presented here have been peak normalized. This normalization means that comparison of different spectra based on apparent integrated intensity or peak height is not possible since these properties are not indicated by the plots even though the underlying calculations contain such information. When varying the optical density of simulated 2DFT spectra, only the strength of the linear response, the source of certain propagation distortions, is modified. The nonlinear response is held constant, meaning that changes in optical density do not affect the strength of signal generation within the sample. Experimentally, this would require a sample in which the nonlinear response comes from a different chromophore than the linear response so that they could be varied independently.

The time-referenced 2DFT rephasing spectra in Figure 3 illustrate the effects of increasing OD and can be compared to the experimental spectra in Figure 3 of ref 57, but have one difference: $T = 500$ fs in the calculation vs. $T = 200$ fs in the experiment. To ease comparison, the limits for both frequency axes in Figure 3 (and in most 2DFT spectra presented here) exactly match those of Figure 4 in ref 57, as can be readily seen from the absolute cyclic frequencies marked at the top of Figure 3. The undistorted 2DFT spectrum in Figure 3a exhibits a star-shaped 2D Lorentzian lineshape which is symmetric in width between the ω_τ and ω_t dimensions, both of which directly reflect the underlying dipole decay rate (see eq 28). This

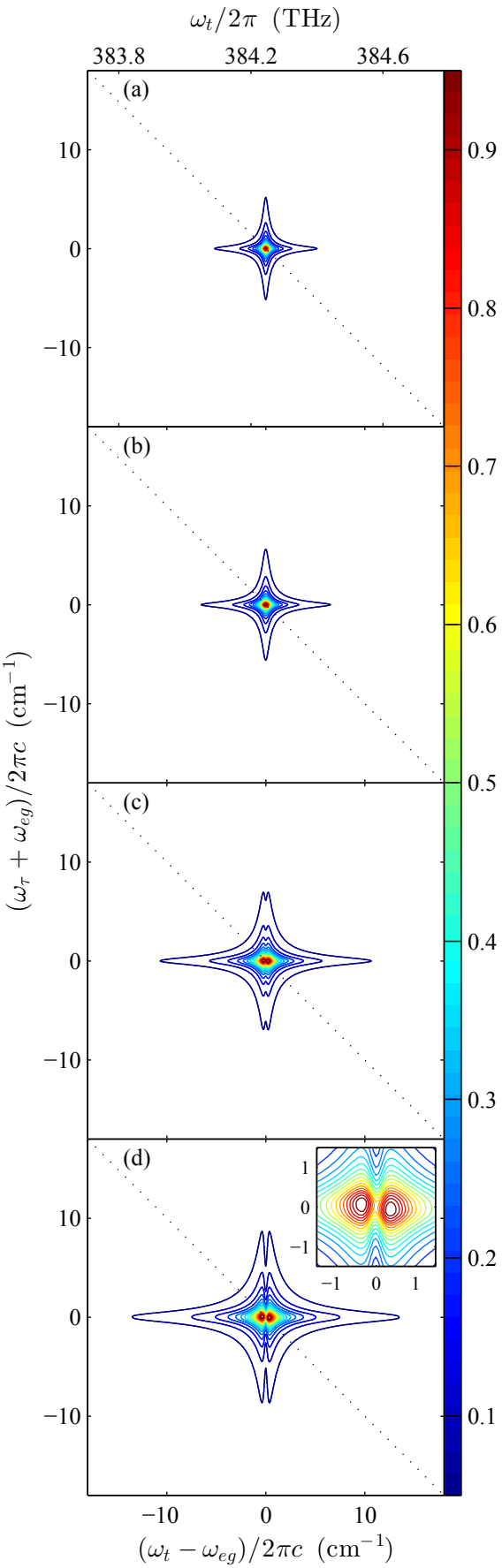

Figure 3: Absolute value rephasing 2DFT spectra ($R\hat{S}^t_{\mathrm{2D}}$ representation) for Bloch model with peak optical densities of (a) 0, (b) 0.14, (c) 0.59, and (d) 1.14. grid time step, 500 fs; grid size, 1024^3; dephasing rate, $\Gamma/2\pi c = 0.265\ \mathrm{cm}^{-1}$; excited state lifetime, $T_1 = 30$ ns; center frequency, $\omega_{eg}/2\pi c = 12816.7\ \mathrm{cm}^{-1}$; waiting time, $T = 500$ fs; sample thickness, $L = 500\ \mu$m; and crossing angles, $\alpha = \beta = 4.84°$. There are 19 contours, evenly spaced every 5% from 5% to 95%. The dotted line indicates the diagonal: $\omega_t = -\omega_\tau$. The inset in (d) is an expanded view of the peak center. The cyclic frequency axis markers and labels at the top show that the limits for both frequency axes are the same as those of Figure 4 in ref 57.

symmetry is a property of absolute value rephasing 2DFT spectra and is not observed in absolute value 2DFT relaxation spectra, which include both positive and negative τ values and are naturally narrower in ω_τ. While increasing the optical density in the subsequent spectra of Figure 3 causes the lineshape to broaden in both dimensions, the width in ω_t increases at a greater rate than that in ω_τ. The resulting lineshape asymmetry, barely visible at a peak optical density of 0.14, is pronounced by the time the optical density reaches 0.59. Although the $\mathrm{OD}_{\mathrm{max}} = 0.14$ spectrum is arguably in agreement with the undistorted spectrum, by $\mathrm{OD}_{\mathrm{max}} = 0.59$ this is clearly not the case as the lineshape in Figure 3c has been broadened considerably and also shows signs of peak splitting due to an absorptive distortion at $\omega_t \approx \omega_{eg}$. The $\mathrm{OD}_{\mathrm{max}} = 1.14$ spectrum is broader still and its peak is split in the ω_t dimension down to the 70% contour. Looking closely at the line center in the inset of Figure 3d, there is a subtle clockwise twisting of the lineshape, whereby the two halves of the split peak have rotated towards the diagonal and are no longer displaced from each other just along ω_t, but also slightly along ω_τ. This may arise from an effect known as "phase-twist"[4,14] which, for an undistorted homogeneous optical Bloch lineshape, occurs only at $T = 0$ and is the result of mixing between the absorptive and dispersive components of the lineshape.[82]

Lifetime and Waiting Time Dependence of Propagation Distortions

The 2D lineshape of an optically thin sample with Bloch model dynamics has no waiting time (T) dependence outside of pulse overlap due to the lack of frequency memory. However, samples with finite optical density distort their excitation pulses, spreading them out in time in a frequency-dependent way, such that time intervals between field–matter interactions within the sample (and even their time-ordering) are not necessarily the same as for the excitation pulses at the sample entrance, introducing distortions of the 2D lineshape that are dependent on both the waiting time (T) and the excited state lifetime (T_1). These coherent transient effects are most pronounced when T and T_1 are on the order of T_2 such that a non-negligible component of the linear free-induction decay from pulses a and b persists through the waiting period until the arrival of pulse c. These additional coherent transient propagation distortions can be shown to vanish so that only incoherent propagation distortions remain at long T (i.e. $T \gg T_2$) in the limit that $2T_1 \gg T_2$, at which point lifetime dephasing is no longer competitive with pure dephasing.

An unintuitive consequence of this phenomenon is that the signal at off-resonant frequencies can be

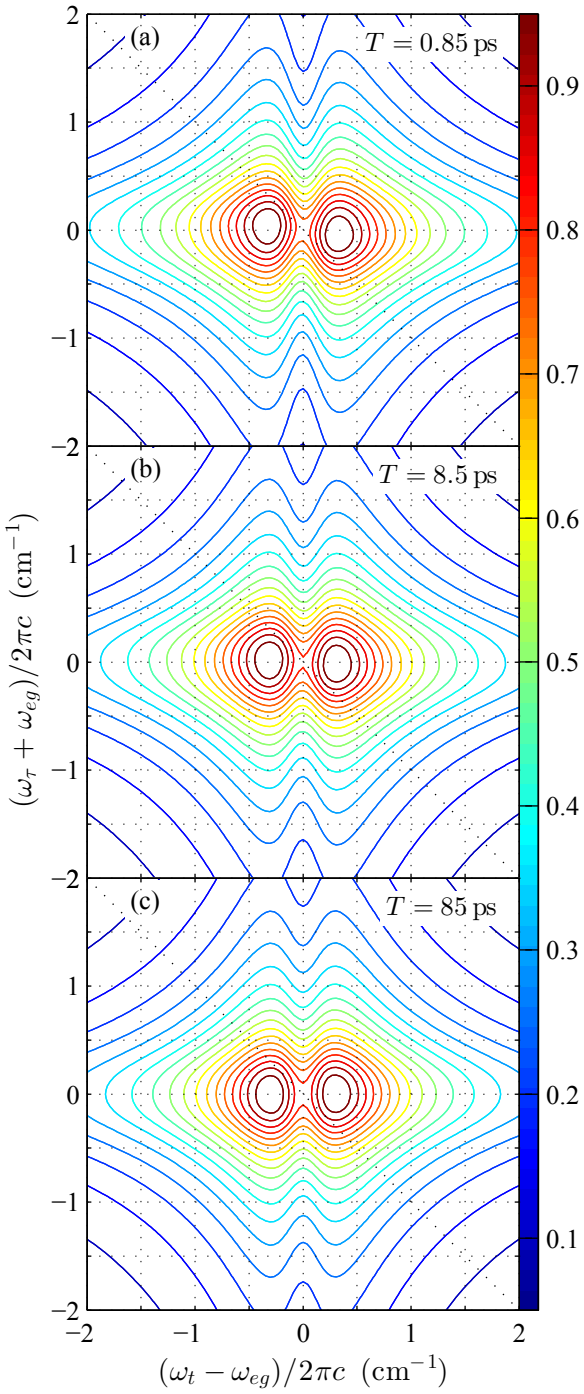

Figure 4: Absolute value rephasing 2DFT spectra ($R\hat{S}^t_{\mathrm{2D}}$ representation) for Bloch model with waiting times a) $T = 0.85$ ps, b) $T = 8.5$ ps, and c) $T = 85$ ps. Peak optical density, $\mathrm{OD}_{\mathrm{max}} = 1$; grid time step, 850 fs; grid size, 1024^3; dephasing rate, $\Gamma/2\pi c = 0.265$ cm^{-1}; dephasing time, T_2 $(= 1/\Gamma) = 20$ ps; excited state lifetime, $T_1 = 240$ ps; center frequency, $\omega_{eg}/2\pi c = 12816.7$ cm^{-1}; sample thickness, $L = 500$ μm; and crossing angles, $\alpha = \beta = 4.84°$. There are 19 contours, evenly spaced every 5% from 5% to 95%. The dotted line indicates the diagonal: $\omega_t = -\omega_\tau$. Dotted grid lines mark 0.5 cm^{-1} increments.

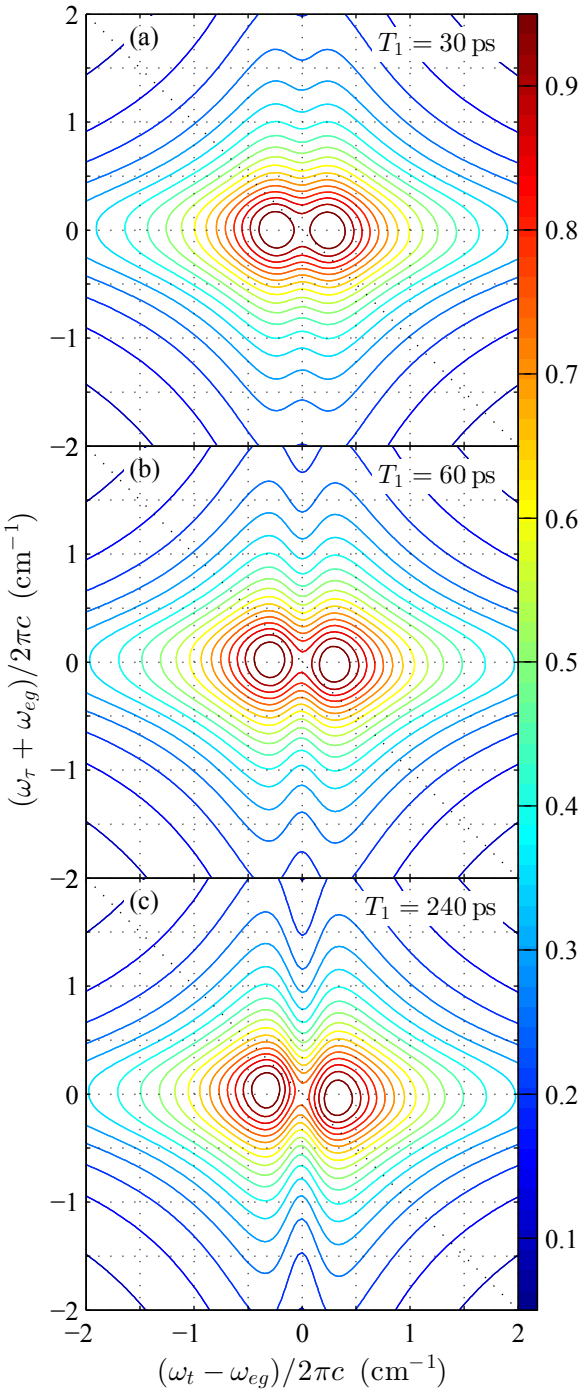

Figure 5: Absolute value rephasing 2DFT spectra ($R\hat{S}^t_{\mathrm{2D}}$ representation) for Bloch model with excited state lifetimes a) $T_1 = 30$ ps, b) $T_1 = 60$ ps, and c) $T_1 = 240$ ps, all at waiting time $T = 0.85$ ps. Peak optical density, $\mathrm{OD}_{\mathrm{max}} = 1$; grid time step, 850 fs; grid size, 1024^3; dephasing rate, $\Gamma/2\pi c = 0.265$ cm^{-1}; dephasing time, $T_2 (= 1/\Gamma) = 20$ ps; center frequency, $\omega_{eg}/2\pi c = 12816.7$ cm^{-1}; sample thickness, $L = 500$ μm; and crossing angles, $\alpha = \beta = 4.84°$. There are 19 contours, evenly spaced every 5% from 5% to 95%. The dotted line indicates the diagonal: $\omega_t = -\omega_\tau$. Dotted grid lines mark 0.5 cm^{-1} increments.

absolutely larger for a sample with a larger linear attenuation compared to a sample with a smaller linear attenuation but the same nonlinear response. As long as the excited state lifetime and the waiting time are of similar magnitudes, the wings of a distorted 2DFT spectrum can be enhanced compared to an undistorted 2DFT spectrum.

Figure 4 illustrates the waiting time (T) dependence of the absolute value rephasing 2DFT spectra for an optically thick sample at a fixed value of T_1. Three distinct effects can be noted. First, the diagonal twisting of the split peak decreases with increasing T. This is expected since phase-twist occurs during pulse overlap (i.e. from $T = 0$ until $T \gg T_2$). Second, the lineshape subtly narrows along the ω_t dimension with increasing T, a signature which is most apparent in the lower contours. Third, and perhaps most interesting, the depth of the absorptive distortion at $\omega_t \approx \omega_{eg}$ decreases as T increases. Going from $T = 0.85$ ps to $T = 85$ ps, the valley at $\omega_t \approx \omega_{eg}$ becomes shallower by about one 5% contour. This suggests that the severity of absorptive distortions at line center might be reduced by measuring 2DFT spectra at longer T where the trailing FID from pulses a and b is no longer present.

The excited state lifetime (T_1) dependence of 2DFT spectra at $T \ll T_2$ is presented in Figure 5. The same three effects observed in Figure 4 are also seen here. However, the scaling of these features with T_1 is the inverse of the scaling with T; as T_1 increases, the ω_t width increases slightly, peak twisting increases, and the absorptive distortion at $\omega_t \approx \omega_{eg}$ deepens. Enhancement of the peak splitting is more pronounced for variation of T_1 in Figure 5, where the splitting deepens by 3 contour levels, than for variation of T in Figure 4, where the splitting loses 1 contour level of depth.

Varying Beam Overlap Through Sample

The decision to include the effects of varying beam overlap was influenced by two observations in comparing the calculations to the experimental spectra[57] at OD > 0.5. First, the aspect ratio of the 2D lineshape in the experimental spectra, represented by the ratio of widths $\Delta\omega_t/\Delta\omega_\tau$, was larger than what could be produced in the calculation by varying OD and Γ. Second, the larger depth of the absorptive distortion along the line $\omega_t \approx \omega_{eg}$ compared to that along the line $\omega_\tau \approx -\omega_{eg}$ in the experimental spectra was indicative of disproportionate attenuation in the ω_t dimension compared to the ω_τ dimension. Although Figure 2 shows that the propagation function already has such an asymmetry, the experimental spectra[57] have an

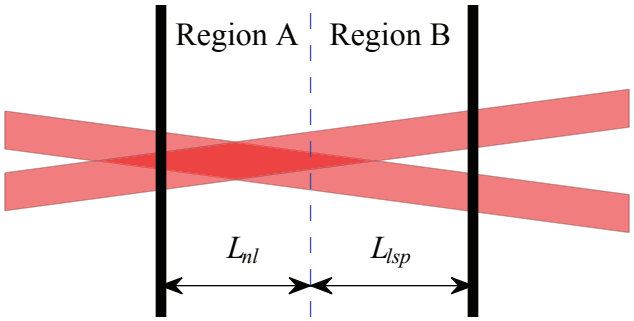

Figure 6: Depiction of beam overlap varying through the sample. Black vertical lines represent the entrance (left) and exit (right) windows. Laser beams are denoted by red parallelograms and only two beams are shown for simplicity. The experimental beam overlap varies continuously between perfect overlap and no overlap as a function of propagation depth into the sample. To gain insight into the qualitative effects to be expected from varying beam overlap, the sample is crudely divided into a region of perfect overlap (A) followed by a region of no overlap (B). In Region A (between the entrance window and the blue dashed line), where excitation beams are well overlapped, the nonlinear signal is generated and propagated over the length L_{nl}. In Region B (between the blue dashed line and the exit window), the nonlinear signal generated in Region A is propagated according to the linear optical properties of the sample over the length L_{lsp} without any further nonlinear signal generation.

even larger difference between the two dimensions.

Varying beam overlap will occur to some extent in any 2DFT experiment involving non-collinear excitation beams with a finite focal spot size and sample path length. If the focal points of the excitation beams spatially coincide, then the beams will completely overlap only in the plane parallel to the windows that contains the focal point. Assuming that the beams cross at the center of the sample cell and that the sample cell length is much shorter than the Rayleigh range,[27] the beam overlap for Gaussian beams with waist w_0 crossing at angle 2α is reduced by a factor of $\exp[-(\tan(\alpha)L/2)^2/w_0^2]$ at the windows. This effect is illustrated in Figure 6, where only two beams are shown for simplicity. Since the focal spot in Figure 6 is nearer to the entrance of the sample cell, the beams are well overlapped in the front portion of the cell, between the entrance window and the blue dashed line, but are poorly overlapped towards the back of the cell, between the blue dashed line and the exit window.

If the position of the sample cell with respect to the common focal point of the excitation beams is adjusted to maximize the intensity of the radiated signal, the focal point will lie nearer to the entrance window for an optically thick sample due to a trade-off between attenuation of all three excitation beams before signal generation versus attenuation of the one signal beam after signal generation. Therefore, we approximate the effect of varying beam overlap as perfect beam overlap in some front portion of the

sample cell and no beam overlap in the remainder as would be expected experimentally when sample cell placement is optimized by maximizing integrated signal intensity. In the crude approximation used here to examine the qualitative effects of varying beam overlap, the fraction of the sample length over which nonlinear signal is generated, given by

$$f_{nl} = \frac{L_{nl}}{L_{nl} + L_{lsp}} \tag{38}$$

can be varied, but the total sample length $L = L_{nl} + L_{lsp}$ is fixed to the thickness of the sample cell.

Since pulse c is linearly propagated before scattering off the grating produced by pulses a and b, the generated signal at each depth is imprinted with this distortion of pulse c before linearly propagating through the remainder of the sample cell.[12] The result is that signal generated at any point in the sample appears as if it were generated at the sample entrance and linearly propagated over the total sample length (as implied by the final exponential of eq 5) such that shape distortions of the 2DFT spectrum along the ω_t dimension are insensitive to changes in the length and location of the signal generation region. However, the linear propagation of pulses a and b prior to signal generation and, consequently, the propagation distortions along the ω_τ dimension are sensitive to such changes, increasing in magnitude as the signal generation region shrinks and moves towards the sample exit.

Implementation in calculation

When implementing this approximate treatment of varying beam overlap, the propagation function Π for Region A should use L_{nl} in place of L and be multiplied by an additional factor of

$$\exp\left\{\mathrm{i}\left[\hat{\mathbf{k}}_d^0(\omega_t)\cdot\mathbf{e}_z\right]L_{lsp}\right\} \tag{39}$$

to incorporate linear propagation of the signal field in Region B. In eq 39, $\hat{\mathbf{k}}_d^0(\omega)$ is the central wave vector of the detection beam in the sample and L_{lsp} is the length of the region in which the signal field is linearly propagated following the nonlinear signal generation region. In addition to the expression in eq 39, an expression is needed that describes the linear propagation of the detection field through region B. This expression is specific to the representation of the spectrum to which it is applied and, therefore, will be defined below for each representation. The linear propagation term in eq 39 and a linear phase evolution

term for the detection field are applied to the FID-referenced representation to yield the varying-beam-overlap FID-referenced rephasing 2DFT spectrum:

$$\begin{aligned} R\hat{S}_{2\mathrm{D}}^{0,\mathrm{VBO}}(\omega_t,\omega_\tau;T) &= R\hat{S}_{2\mathrm{D}}^{0}(\omega_t,\omega_\tau;T) \\ &\quad \cdot \exp\left\{\mathrm{i}\left[\hat{\mathbf{k}}_d^0(\omega_t)\cdot\mathbf{e}_z\right]L_{lsp}\right\} \\ &\quad \cdot \exp\left\{-\mathrm{i}\,\mathrm{Re}\left[\hat{\mathbf{k}}_d^0(\omega_t)\cdot\mathbf{e}_z\right]L_{lsp}\right\} \\ &= R\hat{S}_{2\mathrm{D}}^{0}(\omega_t,\omega_\tau;T) \\ &\quad \cdot \exp\left\{-\,\mathrm{Im}\left[\hat{\mathbf{k}}_d^0(\omega_t)\cdot\mathbf{e}_z\right]L_{lsp}\right\} \end{aligned} \tag{40}$$

For small angles of incidence and $\kappa^2 \ll n^2$, eq 40 can be approximated as

$$\begin{aligned} R\hat{S}_{2\mathrm{D}}^{0,\mathrm{VBO}}(\omega_t,\omega_\tau;T) &\approx R\hat{S}_{2\mathrm{D}}^{0}(\omega_t,\omega_\tau;T) \\ &\quad \cdot \exp\left[-\omega_t\kappa(\omega_t)\ell_{lsp}/c\right] \end{aligned} \tag{41}$$

where $\ell_{lsp} = L_{lsp}/\left(\mathbf{u}\cdot\mathbf{e}_z\right)$ is the additional path length for linear propagation of the detection pulse with unit propagation vector $\mathbf{u}$ through the linear signal propagation length, L_{lsp}. The superscript "VBO" stands for varying beam overlap and indicates that the 2DFT spectrum includes the effects of varying beam overlap distortions. Since the signal and detection fields accrue the same amount of phase when propagating through the linear signal propagation length (L_{lsp}), the phase propagation term on line 3 of eq 40 cancels the oppositely-signed phase propagation contained within the complex exponential term on line 2 of eq 40. This leaves only the attenuation of the signal field over the linear signal propagation length, which is represented by the real-valued exponential terms on the last line of eq 40 (and eq 41).

This distortion can also be applied to the time-referenced representation to yield

$$\begin{aligned} R\hat{S}_{2\mathrm{D}}^{t,\mathrm{VBO}}(\omega_t,\omega_\tau;T) &\approx R\hat{S}_{2\mathrm{D}}^{t}(\omega_t,\omega_\tau;T) \\ &\quad \cdot \exp\left\{\mathrm{i}\omega_t\left[n(\omega_t)-n_v\right]\ell_{lsp}/c\right\} \\ &\quad \cdot \exp\left[-\omega_t\kappa(\omega_t)\ell_{lsp}/c\right] \end{aligned} \tag{42}$$

which is valid for small angles of incidence and $\kappa^2 \ll n^2$ where n is the real part of the refractive index of the sample and $n_v = 1$ is the real-valued refractive index of vacuum. Eq 42 shows that physically,

varying beam overlap introduces two components arising from propagation through Region B: a dispersive component due to the difference in phase accrued by the signal field propagating through L_{lsp} of sample compared to vacuum (line 2) and an absorptive component due to attenuation of the signal field from propagating through L_{lsp} of sample (line 3).

Resulting calculated spectra

The spectra in Figure 7 demonstrate the effect of varying beam overlap where the signal is generated and propagated from the entrance window to a distance L_{nl} into the sample, after which the signal is linearly propagated through the remainder of the sample length (L_{lsp}), as shown in Figure 6. For constant total sample length $L = L_{nl} + L_{lsp}$, the main result of varying beam overlap is to narrow the peak shape in the ω_τ dimension by eliminating some of the linear propagation distortion of pulses a and b. This helps to increase the horizontal-to-vertical aspect ratio of the peak shape in the calculation, bringing it closer to that of the experiment. Twisting of the split peak in Figure 7a is greatly diminished as f_{nl} decreases and is no longer visible by $f_{nl} = 0.2$ (Figure 7c). Varying beam overlap also deepens the absorptive distortion along the line $\omega_t = \omega_{eg}$ except when $T \gg T_2$. Since the signal field is always propagated over the entire sample path length even when signal generation is confined to some front portion of the sample cell, except for coherent effects which may be present when T is *not* very much greater than T_2, changing f_{nl} does not alter the shape of the spectrum in the ω_t dimension as long as the total sample length is held constant.

Excitation–Detection Transformation of Rephasing 2DFT Spectra

When applied to a distorted 2DFT relaxation spectrum (including both positive and negative τ), the excitation–detection transformation[13] to $\hat{S}_{2D}^{++}$ (eq 23) is capable of recovering the ideal (i.e. undistorted) 2DFT relaxation spectrum even for sample optical densities as high as 1. However, as illustrated in Figure 8, applying this transformation to a 2DFT rephasing spectrum does not recover the ideal rephasing spectrum. Given the power and simplicity of the excitation–detection transformation, it is a major disadvantage of 2DFT rephasing spectra that this transformation cannot be directly utilized to obtain the ideal 2DFT rephasing spectrum. The reason for this failure is that while the full τ range 2D time domain signal has some components which are real-valued, even functions of τ, taking only the rephasing (pos-

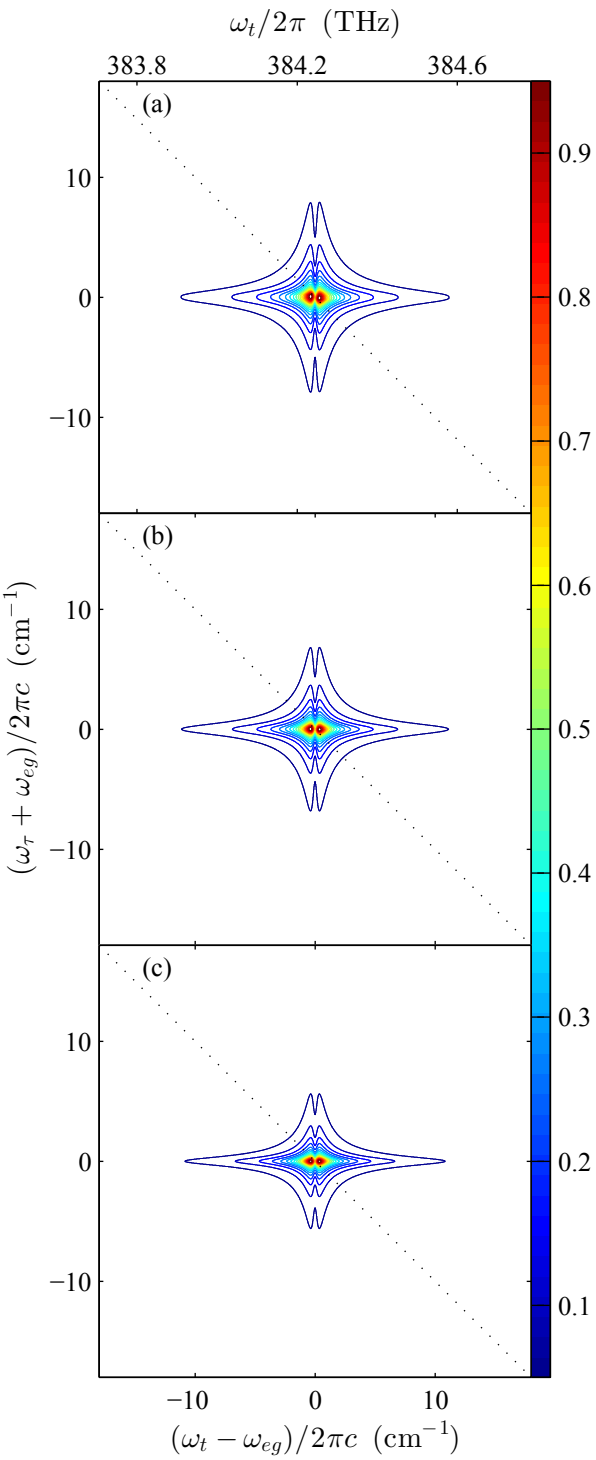

Figure 7: Absolute value rephasing 2DFT spectra ($R\hat{S}^{t,\mathrm{VBO}}_{\mathrm{2D}}$ representation) for Bloch model where signal is generated and propagated through the first (a) 100%, (b) 60%, and (c) 20% of the sample cell and linearly propagated through the remainder. Peak optical density, $\mathrm{OD}_{\mathrm{max}} = 1.14$; grid time step, 850 fs; grid size, 1024^3; dephasing rate, $\Gamma/2\pi c = 0.265$ cm^{-1}; excited state lifetime, $T_1 = 240$ ps; center frequency, $\omega_{eg}/2\pi c = 12816.7$ cm^{-1}; waiting time, $T = 850$ fs; total sample length, $L = L_{nl} + L_{lsp} = 500$ μm; and crossing angles, $\alpha = \beta = 4.84°$. There are 19 contours, evenly spaced every 5% from 5% to 95%. The dotted line indicates the diagonal: $\omega_t = -\omega_\tau$. Both frequency axis limits match those of Figure 4 in ref 57.

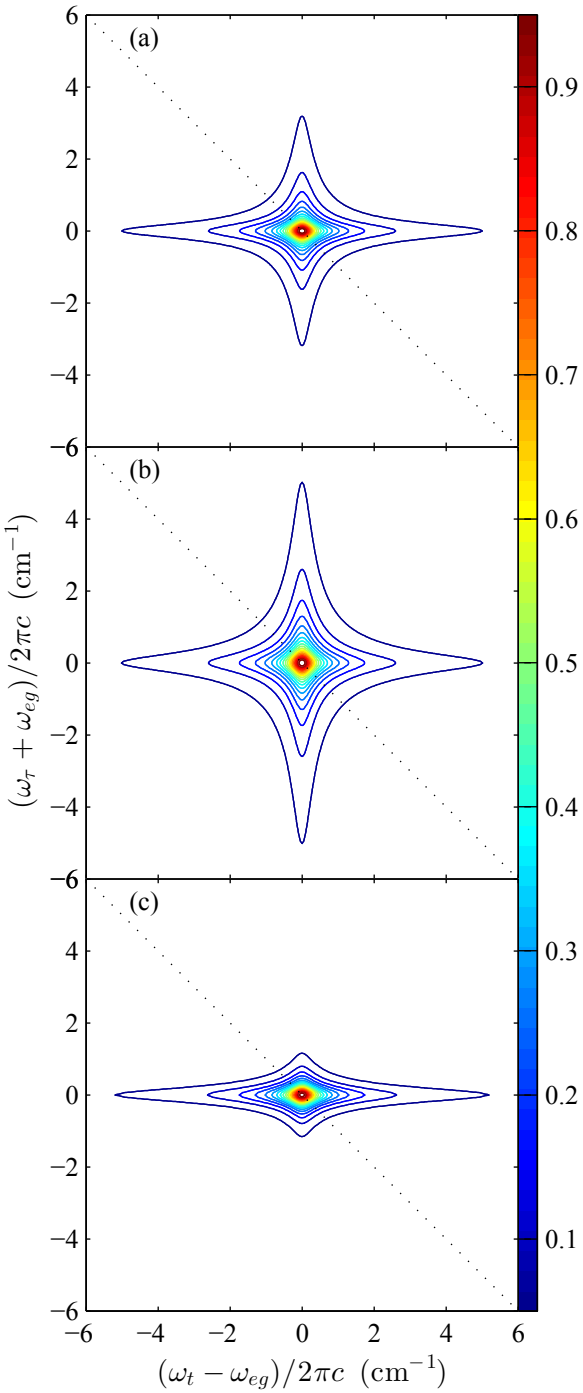

Figure 8: Absolute value 2DFT spectra for a Bloch model. (a) is $R\hat{S}^{++}_{\mathrm{2D}}$ with $\mathrm{OD}_{\mathrm{max}} = 1.14$, (b) is $R\hat{S}^{t}_{\mathrm{2D}}$ with $\mathrm{OD}_{\mathrm{max}} = 0$ (representing the ideal rephasing spectrum), and (c) is $\hat{S}^{t}_{\mathrm{2D}}$ with $\mathrm{OD}_{\mathrm{max}} = 0$ (representing the ideal relaxation spectrum). Note the difference in axis scales when comparing to other figures. Grid time step, 850 fs; grid size, 1024^3; dephasing rate, $\Gamma/2\pi c = 0.265$ cm^{-1}; excited state lifetime, $T_1 = 30$ ns; center frequency, $\omega_{eg}/2\pi c = 12816.7$ cm^{-1}; waiting time, $T = 100.3$ ps; sample thickness, $L = 500$ µm; and crossing angles, $\alpha = \beta = 4.84°$. There are 19 contours, evenly spaced every 5% from 5% to 95%. The dotted line indicates the diagonal: $\omega_t = -\omega_\tau$.

itive τ) part of the spectrum makes half of the real-valued, even components appear to be real-valued, odd functions of τ. When the signal is subsequently Fourier transformed with respect to τ, these artificial real-valued, odd components transform into imaginary-valued, odd components.[81] As is apparent in Figures 8b and 8c, the ideal rephasing spectrum contains signal at values of ω_τ for which there is no signal in the complete 2DFT relaxation spectrum, as illustrated by the lack of signal at the extremes of ω_τ in Figure 8c. When the 2DFT spectrum is truncated at $\tau = 0$, signal amplitude is transfered from near the line center, which is dominated by real components, to the far wings, which are dominated by imaginary components. *Thus the "excitation frequency" in the 2DFT rephasing spectrum does not reflect the physical excitation frequency*.

This rearranged signal is not amplified appropriately by the excitation–detection transformation since it appears at the wrong excitation frequency. The result is that the $R\hat{S}^{++}_{2D}$ spectrum (Figure 8a) neither matches the ideal rephasing spectrum (Figure 8b) nor the ideal relaxation spectrum (Figure 8c). While all three spectra in Figure 8 have similar linewidths in the ω_t dimension, when comparing the linewidths in the ω_τ dimension, the $R\hat{S}^{++}_{2D}$ spectrum is narrower than the ideal rephasing spectrum and yet wider than the ideal relaxation spectrum. The overall narrowest lineshape is found in the ideal $\hat{S}^{t}_{2D}$ spectrum in Figure 8c, which—unlike the ideal rephasing spectrum—is easily recovered using the excitation–detection transformation on $\hat{S}^{0}_{2D}$ with peak optical densities in excess of 1 as long as $T \gg T_2$. At $T = 100.3$ ps, the $\hat{S}^{++}_{2D}$ spectrum with $\mathrm{OD}_{\mathrm{max}} = 1.14$ and the same parameters as in Figure 8 (not shown) has contours which are visually indistinguishable from the ideal $\hat{S}^{t}_{2D}$ spectrum, the two differing by no more than 0.08% (relative to the peak of the spectrum) at any point.

At shorter waiting times, the propagation function is no longer well described by a 2-dimensional function. Despite this complication, the excitation–detection transformation still performs well when applied to 2DFT relaxation spectra at short T.[13] For example, at $T = 850$ fs, the $\hat{S}^{++}_{2D}$ spectrum with $\mathrm{OD}_{\mathrm{max}} = 1.14$ (not shown) and the ideal $\hat{S}^{t}_{2D}$ spectrum (which is identical to Figure 8c) differ by no more than 13% (relative to the peak of the spectrum), the majority of the disagreement occurring near the line center where T-dependent peak twist is most pronounced. In contrast, the same comparison done using 2DFT rephasing spectra results in a difference of up to 20% between a $R\hat{S}^{++}_{2D}$ spectrum with $\mathrm{OD}_{\mathrm{max}} = 1.14$ (not shown) and an "ideal" $R\hat{S}^{t}_{2D}$ spectrum with $\mathrm{OD}_{\mathrm{max}} = 0$ (which is identical to Figure 8b). We note that $\hat{S}^{++}_{2D}$ relaxation spectra may be Fourier transformed to the time domain and truncated to provide an

indirect route to more nearly ideal 2DFT rephasing spectra.

Pseudo–Time Domain Filtering

When viewed in the pseudo–time domain (Fourier conjugate domains to ω_t and ω_τ), representations other than $R\hat{S}^t_{2D}$ and $\hat{S}^t_{2D}$ have signal that appears to arrive at the sample exit before pulse c. The source of this apparent "non-causal" signal is that the detection waves used in these other representations are not true time references due to their propagating through the sample and taking on dispersion that is unaccounted for. While the phase accrued by the detection wave from traversing the sample serves to cancel that accrued by the signal, the variable conjugate to ω_t has been "shuffled" so that it is no longer a true time that can be used to discern the time-ordering of events. While the time ordering of and time delay between pulses are experimentally controllable, the timing of electric field–chromophore interactions are not. Therefore, in the case of an optically thick sample that reshapes the excitation, detection, and signal fields, a given experimental pulse sequence with known pulse timings will have signal contributions from a range of electric field–chromophore interaction intervals and orderings. The larger the temporal smearing of excitation and detection pulses, the larger the range of electric field–chromophore interaction intervals and orderings contributing to the signal. The term "pseudo–time domain" is invoked since this filter is applied along a time dimension that is referenced to an experimental pulse phase which—except for the case of collinear beams, delta-function pulses, and a thin sample—does not specify a unique interaction time and ordering. Therefore, these axes do not necessarily represent true elapsed time and are more properly viewed as the Fourier conjugates of ω_t and ω_τ.

An interesting consequence of the loss of apparent causality in $R\hat{S}^0_{2D}$ is that it may also provide a means to reduce absorptive distortions of the signal field, which are not accounted for in $R\hat{S}^0_{2D}$. It was first observed experimentally by Li et al.[57] that applying a pseudo–time domain filter that truncates the signal before pulse c reduces the appearance of absorptive distortions in the ω_t dimension. The result of applying such a filter to a calculated $R\hat{S}^0_{2D}$ spectrum is illustrated in Figure 9. To produce Figure 9c, an $R\hat{S}^0_{2D}$ spectrum (Figure 9b) has been Fourier transformed into the pseudo–time domain, multiplied by $\theta(t)$, and then Fourier transformed back into the frequency domain. This procedure is consistent with the processing of experimental data illustrated in Figure 4c of ref 57. The filter narrows the spectrum in the ω_t dimension

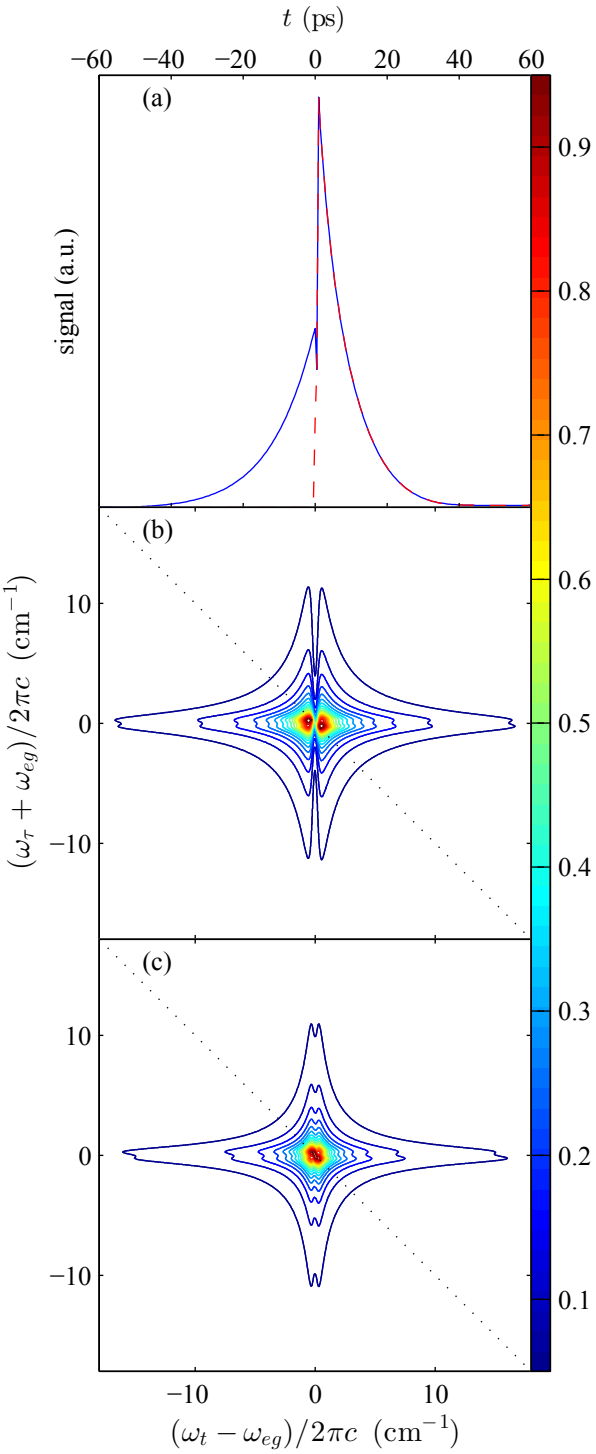

Figure 9: The Bloch model $R\hat{S}^0_{2D}$ 2DFT spectrum Fourier transformed into the pseudo–time domain and integrated over τ (a), with (dashed red) and without (solid blue) pseudo–time domain filtering. The resulting absolute value rephasing 2DFT spectra, (b) without and (c) with pseudo–time domain filtering. Plots (a) and (c) here are comparable to the experimental plots found in Figures 4a and 4c of ref 57, respectively. Peak optical density, $\mathrm{OD}_{\mathrm{max}} = 2.17$; grid time step, 500 fs; grid size, 1024^3; dephasing rate, $\Gamma/2\pi c = 0.265\ \mathrm{cm}^{-1}$; excited state lifetime, $T_1 = 30$ ns; center frequency, $\omega_{eg}/2\pi c = 12816.7\ \mathrm{cm}^{-1}$; waiting time, $T = 500$ fs; sample thickness, $L = 500$ μm; and crossing angles, $\alpha = \beta = 4.84°$. There are 19 contours, evenly spaced every 5% from 5% to 95%. The dotted line indicates the diagonal: $\omega_t = -\omega_\tau$. Both frequency axes in (b) and (c) have scale limits that exactly match those of Figure 4 in ref 57.

and greatly reduces the absorptive distortion at $\omega_t \approx \omega_{eg}$ without significantly altering other aspects of the lineshape. While the validity of such a filtering procedure is not without question, its reduction of absorptive distortions thought to arise from propagation of the signal is immediately apparent. However, a better approach would be to measure the full 2DFT relaxation spectrum and perform the excitation–detection transformation since this procedure most accurately recovers the undistorted spectrum, whose linewidth and lineshape are physically reflective of the microscopic dipole dynamics.

Discussion

Although differences remain, the simulations qualitatively reproduce many different propagation distortions of the experimental 2DFT spectra,[57] including varying beam overlap distortions and peak shape broadening, splitting, and twist. As mentioned in the Introduction, prior studies of Rb photophysics suggest that the experimental 2DFT spectra will contain contributions with large waiting times (repetitive excitation) and short lifetimes (alignment); both will quantitatively reduce peak splitting and twisting. Additionally, the effects of pseudo–time domain filtering, in both t and τ dimensions, have been modeled and the trade-offs of using these filters have been addressed. In this section, comparisons between simulated and experimental 2DFT spectra will be further developed, highlighting both areas of agreement and disagreement as well as suggesting experimental methods which minimize propagation distortions and facilitate theoretical modeling. Finally, we discuss strategies for decoupling propagation distortions and the nonlinear optical response of samples at high optical density.

Optical Density Effects

Although the range of linewidths observed when varying the optical density from 0.14 to 1.14 in Figure 3 of ref 57 is larger than the range for simulations in Figure 3, both show that increasing the optical density of a sample increases its linewidth in addition to altering its lineshape. Both experimental and simulated 2DFT spectra exhibit the onset of peak splitting at $\mathrm{OD}_{\mathrm{max}} = 0.59$, the result of strong attenuation of the signal near the resonant frequency (ω_{eg}). Similar optical density–dependent peak shape broadening was previously reported in simulations of absolute value rephasing 2DFT photon echo spectra at zero waiting time by Keusters and Warren [10] and in simulations of complex-valued 2DFT relaxation spectra by

Yetzbacher et al..[13] At the highest optical density, subtle twisting of the split peak in Figure 3d is mirrored in the experimental 2DFT spectrum. The experimental and simulated $OD_{max} = 1.14$ 2DFT spectra also share a significant absorptive distortion around $\omega_t = \omega_{eg}$, although the distortion is more pronounced in the experiment, where it cuts all the way down through the 5% contour level (vs. the 70% contour of the simulation). Discrepancies at high optical density will be discussed further below.

Splitting and twisting of the experimental 2D peak shape at high optical density were predicted by Yetzbacher et al.[13] in a simulation of real (absorptive) 2DFT relaxation spectra, and the observation of these features in absolute value rephasing 2DFT spectra of Rb vapor by Li et al.[57] largely motivated this collaboration. The prior simulation (Figure 5 of ref 13) demonstrates subtle peak splitting and twist in an $\hat{S}^t_{2D}$ 2DFT spectrum for a homogeneous Bloch model in the *lifetime*-dephasing limit at a peak optical density of 0.87. By comparison, the simulations presented in Figure 3 are in the *pure*-dephasing limit of the homogeneous Bloch model where peak splitting and twist are more prominent for the same optical density, an effect discussed further below. At optical densities beyond those explored by Yetzbacher et al., twisting is clearly visible near the center of the peak in Figures 3d, 5c, and 10, which have optical densities ranging from 1 to 3.

Twisting requires a correlation between ω_t and ω_τ. Although the effect of phase-twist on the real part of 2DFT spectra is similar in appearance to the peak shape twist observed here, phase-twist is only observed during pulse overlap (i.e. when $T \approx 0$) in ideal 2DFT spectra. However, with the inclusion of propagation distortions, phase-twist could occur for larger waiting times due to the temporal overlap of pulse c with the trailing FID of pulse a or b. Since phase-twist does not affect peak shapes in ideal absolute value rephasing 2DFT spectra, for it to be responsible for the peak shape twist observed here would require a complicated interaction between phase-twist and propagation distortions, a conclusion consistent with the appearance of peak twist only at relatively high optical density.

Peak splitting is simpler to understand than peak twisting and is the result of resonant absorption of pulses a and b (for splitting in the ω_τ dimension) and pulse c and the signal (for splitting in the ω_t dimension). Just as with peak shape broadening,[10,13] this distortion is more severe along the ω_t dimension than along ω_τ, even in simulations where excitation beams are perfectly overlapped through the entire sample length. This similarity between peak shape broadening and splitting highlights their common source: preferential attenuation of the signal and excitation fields near $-\omega_\tau = \omega_t = \omega_{eg}$.

Waiting Time and Excited State Lifetime Dependence

If the radiated linear free-induction decay from pulses a and b is non-negligible at the end of the waiting period (i.e. $T \not\gg T_2$), propagation distortions will have 3-dimensional features that are not reducible to lower dimensionality. Figures 4 and 5, although without analogs in the experimental work, demonstrate this 3-dimensional nature of propagation distortions by varying the waiting time and excited state lifetime, respectively, at a fixed total dephasing time.

In simulations of absolute value rephasing 2DFT correlation spectra for the homogeneous Bloch model, Keusters and Warren [10] reported asymmetric peak shape broadening at a peak optical density of 0.32, with more severe broadening in the ω_t dimension than in ω_τ. In addition, they found that this asymmetry was larger in the pure-dephasing limit ($T_2 = T_2^*$) than in the lifetime-dephasing limit ($T_2 = 2T_1$). At a higher optical density ($\mathrm{OD}_{\mathrm{max}} = 1$) than studied by Keusters and Warren,[10] our simulations show that—in addition to peak shape broadening—peak shape twist and splitting are also affected by the ratio T_1:T_2. Figure 5 explores intermediate excited state lifetimes compared to the pure- and lifetime-dephasing limits simulated by Keusters and Warren.[10] The trend we observe of larger peak shape broadening asymmetry at a longer excited state lifetime is in agreement with what they report.[10] Not visible in their work at lower optical density is the trend of peak shape twist and splitting with the ratio T_1:T_2, both of which are enhanced at longer excited state lifetimes in Figure 5. These spectra show that the ratio T_1:T_2 is important for an optically dense sample since it controls the fraction of signal generated from interactions with the incident fields of pulses a and b versus their radiated FID. For two pulse photon echoes at low optical density, Keusters and Warren [10] qualitatively explained the broadening as arising from destructive interference between the nonlinear signal generated by interactions with the two main pulses and the signal generated by interactions with the main part of one pulse and the trailing FID of the other pulse. A key aspect of their discussion is that, for a resonant excitation pulse, the trailing FID is π out of phase and decays exponentially in time with the time constant T_2. As a result, nonlinear signal involving one FID interaction can be generated after the main pulse has passed and interfere destructively with the nonlinear signal from interaction with the main part of the pulse, hastening decay of the nonlinear signal field and broadening the spectrum. Discussion for four-wave mixing at low optical density should consider a trailing FID on any one of the four waves (three excitation pulses plus signal). The effect of interacting with the trailing

FID of the first pulse (a) is to broaden the 2DFT spectrum in the ω_τ dimension and is likely to be similar for two pulse and three pulse echoes, as is the effect of interacting with the trailing FID of the last pulse (c) in broadening the 2DFT spectrum in the ω_t dimension. Keusters and Warren [10] suggested that increases in T_1 allow greater contributions from interactions with the FID trailing the last pulse (c), distorting the 2DFT spectrum primarily along the ω_t dimension. Here, similar coherent transient propagation effects are probed at higher optical densities, where interactions with multiple trailing FIDs (each of which may reflect multiple absorption–re-radiation cycles) must be simultaneously considered.

Figure 4 demonstrates that varying the waiting time has similar effects on the 2DFT spectrum as varying the excited state lifetime. Shorter waiting times exhibit more severe peak shape twist, broadening, and splitting. These simulated 2DFT spectra illustrate the importance of the ratio T:T_2. The effect of decreasing the waiting time T in Figure 4 is qualitatively similar to that of increasing the lifetime T_1 in Figure 5, suggesting a common origin. The qualitative explanation of the lifetime effect given by Keusters and Warren [10] is consistent with the waiting time effect.

Given the complexity of propagation distortions in the coherent regime, it is beneficial from the point of view of interpretation and modeling to first characterize the 2DFT spectrum at $T \gg T_2$ before investigating dynamics at shorter waiting times where coherent effects are present. Since simulating a 2DFT spectrum at a long waiting time is typically a 2-dimensional problem, it is more straightforward in this limit to separate microscopic dipole dynamics from propagation distortions and to determine the optical density of the sample from its 2DFT spectrum.

Comparison to Experiment

The absorption lineshape broadening of a gas-phase chromophore can often be factored into homogeneous Lorentzian components—such as non-resonant collisional (or pressure) broadening, resonant self broadening, and lifetime broadening—and inhomogeneous Gaussian components, such as Doppler broadening. Collisional broadening is caused by chromophore–buffer gas collisions while self broadening comes about due to chromophore–chromophore collisions. Based on the literature values [58,87,95,96] of these sources of broadening for Rb in Ar buffer gas, collisional broadening dominates, accounting for greater than 98% of the total linewidth under the conditions of the experiment. [57] This prediction is based on using the ex-

perimental Rb reservoir temperature to determine the vapor pressure[97] and number density of Rb in the sample cell. To estimate collisional broadening, it is assumed that 2 atm of Ar is loaded into the cell at 298 K and that its pressure increases as the cell is heated at constant volume, as in the experiment.[57] It should be noted that there is approximately ±20% variation between sources in the reported Rb vapor pressure curve[97–99] and collisional broadening coefficient.[87,88,98,100–103] However, it appears that such uncertainty is insufficient to account for the differences between the results of calculations and experimental measurements.

At the lowest Rb reservoir temperature (90°C, $OD_{max} = 0.14$), the predicted Lorentzian FWHM linewidth (1.14 cm^{-1}) is more than three times larger than the linewidth estimated from the experimental[57] absorption spectrum (~0.35 cm^{-1}). The disagreement persists at the highest Rb reservoir temperature (160°C, $OD_{max} = 1.14$) where theory predicts a linewidth of 1.25 cm^{-1} while the experimental[57] absorption spectrum indicates a linewidth of ~0.51 cm^{-1}. Owing to the inconsistency between the experimental absorption spectra and these simple theoretic predictions of the lineshape, the dephasing rate used in these simulations was set to $\Gamma = 50$ rad/ns $= (2\pi c)\, 0.265$ cm^{-1}, corresponding to a FWHM of 0.53 cm^{-1}, a compromise between the experimental and predicted linewidth estimates.

In addition, with values for the linewidth,[58,87,95,96] Rb number density,[97] and integrated absorption cross section,[95] the absorption spectrum can be simulated for comparison to experiment. In order to avoid sample cell uptake of Rb, the sample cell[104] is made of a titanium body with sapphire[105] windows. Since this calculation relies on the experimentally reported Rb reservoir temperature to determine the Rb number density in the optical path of the excitation beams, it will fail in the case of an inhomogeneous temperature or Rb vapor distribution throughout the sample cell. While linear absorption measurements are sensitive to the integrated number density of chromophores but not to chromophore density gradients, 2DFT spectra are sensitive to both, and the simulations of 2DFT spectra presented here assume a uniform chromophore distribution in calculating propagation distortions. While the Beer-Lambert law predicts a linear proportionality between optical density and concentration, the plot of experimental optical density vs. concentration calculated from the Rb reservoir temperature is nonlinear and appears to saturate as Rb number density increases. The experimental and calculated OD_{max} coincidentally agree to within 2% at the highest Rb reservoir temperature. Predicted optical densities are a factor of 1.4 to 6.2 lower than experimental ones at all except the highest experimental temperature.

Furthermore, the extent of propagation distortions in the experimental 2DFT spectra implies optical densities higher than measured in the experimental absorption spectra. This difference is evidenced by simulated 2DFT spectra, calculated with optical densities taken from experimental linear absorption spectra, having considerably milder propagation distortions than experimental 2DFT spectra at the same Rb reservoir temperatures. As with the disagreement in linewidth, these inconsistencies cast doubt on the reliability of the experimental absorption measurements as a source of OD_{max} and Γ for 2DFT spectra and also suggest that the Rb reservoir temperature may not be directly indicative of the Rb vapor density in the path of the excitation beams. These discrepancies may result from differences in beam power or buffer gas pressure between measurements of the linear absorption spectrum and the 2DFT spectrum, which were taken on different days.

Before comparing calculated and measured 2DFT spectra, it is important to mention two standard checks on the experiment. First, the excitation pulse energy dependence of the nonlinear signal pulse energy was measured at 5, 7.5, and 10 mW excitation beam power; the best fit exponent was 3.1 ± 0.4, agreeing with a cubic power dependence within error. Second, the maximum single pulse excitation probability was estimated from the pulse area[61] using the transition dipole for linearly polarized D_2 excitation (2.07×10^{-29} Cm). Using the measured pulse duration, pulse energy, and beam diameter, the calculated excitation probability reaches 10% at the center of the beam just inside the sample entrance window. This excitation probability would be consistent with the measured third-order power dependence of the signal if relaxation were complete between pulse sequences, but the absence of known quenching channels suggests some higher-order pumping processes not detected in the experimental power dependence. There could be an unexpected quenching channel or optical pumping might effectively modify the steady-state response,[56,77] adding an uncertainty beyond that arising from uncertainties in optical density. As a result, we decided to vary the optical density used in the simulations to best reproduce the propagation distortions present in the experimental 2DFT spectra.

No asymmetry is present in undistorted (OD = 0) rephasing 2DFT spectra calculated using the homogeneous Bloch model, which produces a symmetric star-shaped peak in absolute value. At the lowest experimental optical density ($OD_{max} = 0.14$), only minor propagation distortions are expected and simulations do not reproduce the asymmetry in linewidth between the ω_τ and ω_t dimensions observed in the experiment. While absorptive distortions broaden lineshapes more severely along ω_t than along ω_τ,

the 2:1 aspect ratio of the $OD_{max} = 0.14$ experimental 2DFT spectrum is only recovered in simulations at $OD_{max} > 1$, by which point peak splitting becomes evident. Figures 4 and 5 indicate that peak splitting will remain when signals expected from repetitive excitation [$T = 13$ ns, $T = 26$ ns, $T = 39$ ns, etc. with exponentially diminishing amplitudes $\exp(-T/T_1)$ and population lifetime $T_1 = 27$ ns] and alignment (with alignment lifetime $T_1 = 20$ ps and one-third the amplitude of the $T = 200$ fs 2DFT spectrum) are included. Both the mean time between Rb–Ar collisions ($\bar{\tau} \approx 10$ ps) and the collision duration ($\tau_c \approx 2$ ps),[107] estimated for the experimental conditions,[57] are longer than the experimental waiting time ($T = 200$ fs). This might lead one to doubt the applicability of the homogeneous Bloch model in favor of the Kubo stochastic model or inhomogeneous Bloch model for this experiment. However, these models produce either a symmetric star-shaped peak, in the case of the Bloch model in the homogeneous limit and the Kubo stochastic model in the fast-modulation limit, or a diagonally-elongated peak that is roughly elliptical, in the case of the Bloch model in the inhomogeneous limit and the Kubo stochastic model in the slow-modulation limit. Calculations by Keusters and Warren[10] for a pure dephasing Bloch model indicate that higher intensity pulses *reduce* propagation asymmetry at $OD_{max} = 0.32$ in the absolute value rephasing 2DFT spectrum; this suggests that high intensity pulses would *not* cause asymmetry at low optical density. On the experimental side, scattered light with intensity less than 2% of the peak shape maximum lies along $\omega_\tau = -1.004\,\omega_t$ and is coincident with the diagonal within the likely uncertainty of this check while potential ghost peaks are below 5% of the peak amplitude of the 2DFT spectrum. The origin of this asymmetry in the 2D peak shape is not understood, perhaps indicating that the two-level homogeneous Bloch model is not adequate to describe the nonlinear optical response of this system.

Comparing "reference around" experimental 2DFT spectra by Li et al.[57] to simulated 2DFT $R\hat{S}^t_{2D}$ spectra using the experimentally reported values for $OD_{max} = (0.14, 0.59, 1.14)$ and $f_{nl} = 0.8$, clear disagreement in the width of the 2DFT lineshape and the depth of the absorptive distortion near $\omega_t = \omega_{eg}$ is noted. While reducing the fraction of the sample in which the signal field is generated (Figure 7) does increase the aspect ratio of the 2D lineshape and slightly deepens the absorptive distortion near $\omega_t = \omega_{eg}$, it does nothing to increase the linewidth in the ω_τ dimension, which is needed to better match the experimental spectra. Outside of the dephasing rate, which is already set to a larger value than observed in the experimental linear absorption spectrum, optical density is the only handle for changing the ω_τ width. To recover the ω_τ width of the experimental OD = 1.14 "reference around" spectrum (Figure 3 of ref 57),

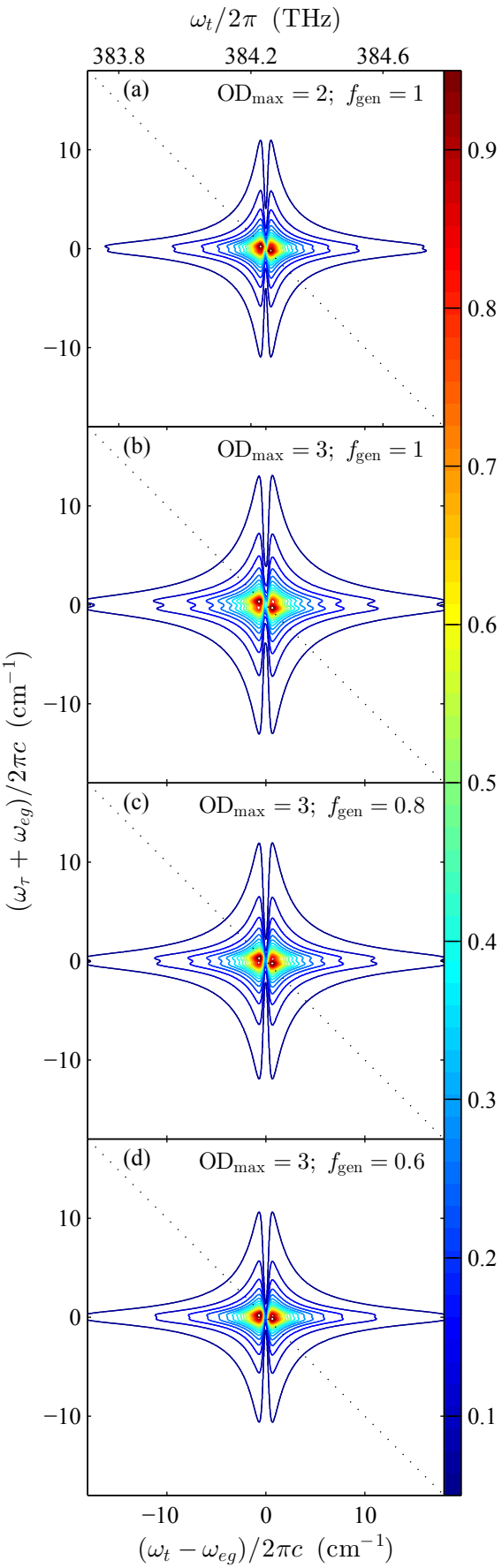

Figure 10: Absolute value rephasing 2DFT spectra with additional signal propagation ($R\hat{S}_{\mathrm{2D}}^{t,\mathrm{VBO}}$ representation) for Bloch model with (a) $\mathrm{OD}_{\max} = 2$, $f_{nl} = 1$; (b) $\mathrm{OD}_{\max} = 3$, $f_{nl} = 1$; (c) $\mathrm{OD}_{\max} = 3$, $f_{nl} = 0.8$; and (d) $\mathrm{OD}_{\max} = 3$, $f_{nl} = 0.6$ where $f_{nl} = L_{nl}/(L_{nl} + L_{lsp})$ is the fraction of the sample length over which nonlinear signal is generated. Grid time step, 500 fs; grid size, 1024^3; dephasing rate, $\Gamma/2\pi c = 0.265\ \mathrm{cm}^{-1}$; excited state lifetime, $T_1 = 240$ ps; center frequency, $\omega_{eg}/2\pi c = 12816.7\ \mathrm{cm}^{-1}$; waiting time, $T = 500$ fs; sample thickness, $L = L_{nl} + L_{lsp} = 500$ μm; and crossing angles, $\alpha = \beta = 4.84°$. There are 19 contours, evenly spaced every 5% from 5% to 95%. The dotted line indicates the diagonal: $\omega_t = -\omega_\tau$. The absolute cyclic frequency axis at the top of the figure indicates that both frequency axes have scales exactly matching those of Figure 4 in ref 57.

the OD_{max} used in the simulation was increased to ~3, as illustrated in Figure 10. Since a ~25 K increase in temperature of the Rb vapor sample cell is sufficient to cause a factor of 3 increase in the number density of Rb, a 3-fold increase in optical density might be within the combined uncertainty of the temperature and linear absorption measurements. Optical pumping[77] and local heating of the sample by the excitation beams[108] might also contribute to the disagreement in lineshape. Given the likely uncertainty in optical density, model values of $OD_{max} \approx 3$ and $f_{nl} \approx 0.8$ may best represent the actual experimental conditions. Comparing the $OD_{max} = 1.14$ experimental 2DFT spectrum in Figure 3 of ref 57 to the $OD_{max} = 3$ simulation in Figure 10c, the FWHM through the left and right maxima along the excitation dimension are 2.1 cm^{-1} and 2.4 cm^{-1} (experiment) vs. 2.4 cm^{-1} and 2.4 cm^{-1} (simulation), the line-center FWHM along the detection dimension are 3.9 cm^{-1} (experiment) vs. 4.6 cm^{-1} (simulation), the line-center splitting FWHM along the detection dimension are 0.83 cm^{-1} (experiment) vs. 0.65 cm^{-1} (simulation), the splitting depths (as a fraction of the peak shape maximum) are 0.016 (experiment) vs. 0.273 (simulation), and the split peaks are twisted from the horizontal toward the diagonal by 10° (experiment) vs. 22° (simulation). While the effect of any optical pumping has not been calculated, adding signal contributions from repetitive excitation (with long waiting times as in Figure 4c) and alignment (with a short lifetime as in Figure 5a) would reduce split peak twisting in the simulation, bringing it into closer agreement with experiment. This rough agreement for the split peak twisting provides a crucial check of propagation distortion theory in the coherent transient regime.

Implications for Experiment

Yetzbacher et al. previously outlined experimental conditions in which propagation distortions are minimized and introduced transformations that reduce distortions in 2DFT correlation and relaxation spectra at optical densities of up to 1.[13] Through characterization of pseudo–time domain filtering, which includes filtering both in τ (to produce rephasing 2DFT spectra) and in t, it appears that these filtering techniques provide no clear advantage over application of the excitation–detection transformation to 2DFT relaxation spectra for recovering the ideal lineshape. The $\hat{S}_{2D}^{++}$ spectrum not only matches the ideal 2DFT relaxation spectrum (Figure 8c) to a high degree, but it also has a narrower 2D lineshape than the $R\hat{S}_{2D}^{++}$ spectrum (Figure 8a). However, any well-characterized pseudo–time domain filter can be applied to simulations

using the 3DFT method, as exhibited in Figures 8 and 9. The effect of a pseudo–time domain filter that removes signal that appears to arrive before pulse c in the t dimension, presented in Figure 9, matches some of the experimental signatures of this filter in Figure 4 of ref 57. In particular, simulations capture both the narrowing of the lineshape in ω_t and the reduction in the depth of the absorptive distortion near $\omega_t = \omega_{eg}$.

Despite the crude nature of the approximation used, our treatment of varying beam overlap was able to capture the experimental signature of this distortion wherein the aspect ratio of the 2D lineshape is larger than that produced by the propagation function alone. This analysis also illustrates two important points. First, it reinforces the observation that the signal is always effectively propagated over the entire length of the sample cell regardless of where it is generated within the sample cell.[12] As evidence, it can be seen in Figure 7 that reducing the length of the region over which signal generation occurs does not alter the lineshape in the ω_t dimension as long as the total sample length is held constant. Second, it shows the disadvantage of using a sample cell with a path length longer than the overlap length of the incident laser beams since any region where beams are not well overlapped will not contribute significantly to signal generation, but will attenuate and distort the signal.

A pseudo–time domain filter around $t = t_c \equiv 0$ was used in the work by Li et al.[57] to discriminate against scatter from excitation pulses. Simulations of "reference around"-type $R\hat{S}^t_{2D}$ 2DFT spectra exhibit a strong dependence on the exact placement of this filter. Moving the filter by 1 ps into positive t causes the height of the spectrum at $\omega_\tau = \omega_t = \omega_{eg}$ (relative to the peak of the spectrum) to decrease by a factor of 3, greatly enhancing the depth of the absorptive distortion. This sensitivity indicates that even a small uncertainty in the position of a pseudo–time domain filter around $t = 0$ can significantly alter the 2DFT spectrum.

Using the method put forward by Hybl et al.,[3] 2DFT spectra at long waiting times ($T \gg T_2$) can be simulated with no adjustable parameters, relying only on independent 1D spectra of the sample and excitation pulses. Such simulations are valuable for comparison to experimental 2DFT spectra in the long T limit. They can also be compared to 2DFT spectra simulated by the 3DFT method in order to test lineshape models and to estimate the magnitude of propagation distortions. Furthermore, experimental 2DFT spectra taken under conditions where the optical density and lineshape model, as well as its parameters, can be predicted from prior literature results provide the opportunity to simulate distorted 2DFT spectra

with no adjustable parameters even at short waiting times where coherent effects are present in both the 2D peak shape and the propagation distortions.

Distorted 2DFT spectra at short waiting times often disguise their true peak shape and peak width under coherent effects and absorptive line broadening, making them a poor source of information on which to base simulations. If the Bloch model is truly appropriate (and there are physical grounds to doubt this at waiting times less than the time between collisions or the collision duration), all of the parameters necessary for the 3DFT simulation are available from the experimental geometry and independent spectroscopic measurements. So, for cases where there is no reliable source of lineshape information in the literature, simulations of distorted 2DFT spectra at arbitrary T with no adjustable parameters may still be possible.

Through the challenge of modeling extreme propagation distortions, this study suggests a set of measurements to aid quantitative theoretical modeling. Measurement of the free-induction decay of each of the excitation pulses can check linear propagation of the excitation fields, which is a requirement of the theory underlying these calculations. Linearity of absorption, however, does not guarantee linear propagation.[3,12,28] Well-resolved linear absorption spectra are also critical to this check. As with free-induction decay measurements, absorption spectra indicate the optical density of the sample and, for the homogeneous Bloch model, determine the lineshape function. The theory requires that excitation beam overlap homogeneously fill the entire sample path length, which can be accomplished by either using shallow beam crossing angles or a sufficiently thin sample cell. For the homogeneous Bloch model, 2DFT relaxation spectra measured at $T \gg T_2$ and low optical density can independently determine the lineshape parameters since coherent effects are minimized at long T, leaving a "product-lineshape" which is simpler to interpret. For a detailed analysis of 2DFT spectra at long waiting times, see the appendix of ref 3. 2DFT relaxation spectra at $T \gg T_2$ but with higher optical densities, once corrected for propagation distortions using the excitation–detection transformation (exact when $T \gg T_2$), would reveal the dependence of homogeneous Bloch model parameters on chromophore density. Although increasing the optical density by increasing the temperature in this experiment would also increase the relative Rb–Ar velocity and hence the dephasing rate, the predicted ~10% increase in linewidth from 363 K to 433 K due to Rb–Ar collisions is small compared to the line broadening caused by propagation distortions over the same range. Alternatively, long-T spectra could serve an an independent measurement of the sample optical density if the lineshape model parameters are known from an independent source. These measurements and exper-

imental checks enable unambiguous assignment of a lineshape model, lineshape parameters, and optical density in the incoherent limit and serve as a foundation for modeling the addition of coherent effects at short waiting times.

Conclusions

Absolute value rephasing 2DFT spectra of the collision-broadened D_2 line of rubidium in argon buffer gas have been simulated over a range of optical densities using a 3DFT method[11–14] and compared to experimental 2DFT spectra reported by Li et al.[57] The slightly temperature-dependent Lorentzian linewidths predicted from previously measured Rb–Ar collision cross sections[58,87] indicate that propagation distortions are responsible for nearly all of the change in optical Bloch model 2D peak shapes across the experimental range of optical densities. When the waiting time is much greater than the dephasing time, propagation distortions of the 2DFT relaxation spectrum reduce to a 2D propagation function that is separable into a product of 1D excitation frequency (ω_τ) and detection frequency (ω_t) attenuation factors, divided by a 1D refractive factor. When the waiting time T is less than the dephasing time T_2, the optical Bloch model is no longer separable into independent ω_τ, ω_t, and T dimensions. In this coherent transient regime, propagation distortions reveal the three-dimensional nature of the third-order nonlinear susceptibility and response explored here.

Although absolute value rephasing 2DFT spectra for the optical Bloch model have a symmetric 2D Lorentzian star shape in the low OD limit, increases in the optical density of 2DFT spectra initially generate a 2D Lorentzian peak shape with a greater linewidth along the detection frequency (ω_t) than the excitation frequency (ω_τ).[10] This occurs for two reasons: more signal is generated near the front of the sample, at depths where pulses that dictate the excitation frequency are less attenuated; in contrast, the attenuation of the last excitation pulse and of the signal combine to generate an effective attenuation of the detected signal throughout the entire sample length, independent of the depth at which signal is actually generated.[12]

The above differences between lineshape distortions along the excitation and detection frequency dimensions are magnified when the excitation beams do not overlap throughout the sample, as in the Rb 2DFT experiment.[57] For a fixed total sample length, maximum signal is generated by maximizing beam

overlap near the entrance window–sample interface. Decreasing the length of the beam overlap region at fixed total sample length decreases absorptive distortions along the excitation frequency dimension while leaving signal attenuation and distortion along the detection frequency largely unchanged. Matching the sample and beam overlap lengths is recommended to enhance signal and reduce distortion.

At peak optical densities greater than 0.5, peak splitting around the resonant detection frequency is observed in both experimental and simulated 2DFT spectra. Higher optical densities produce further increases in linewidth, deeper peak splitting, and introduce progressive peak shape twisting below $OD_{max} = 1$. As the waiting time T increases, the detection frequency linewidth slightly decreases, peak splitting diminishes, and peak twist disappears. The opposite trends are observed when increasing the excited state population lifetime T_1.

An excitation–detection transformation[13] exactly recovers the ideal 2DFT relaxation spectrum at waiting times T much greater than the dephasing time T_2 and still approximately recovers the ideal spectrum at shorter waiting times. In contrast, the ideal 2DFT rephasing spectrum is not recovered by the same transformation of a rephasing 2DFT spectrum. Although time domain filters reduce distortion of the rephasing 2DFT spectrum, we note that distortion of the rephasing 2DFT spectrum can be reduced (for short T) or eliminated (for $T \gg T_2$) by extracting the rephasing 2DFT spectrum from the excitation–detection transformed 2DFT relaxation spectrum, which contains both rephasing and non-rephasing 2DFT spectra. Long waiting time 2DFT relaxation spectra are recommended for verifying sample conditions.

Simulations of absolute value rephasing 2DFT spectra using a peak optical density of 3, a collisional broadening linewidth of 0.5 cm^{-1}, and beam overlap in the first 80% of the sample closely resemble the experimental "reference around" 2DFT spectra reported for $OD_{max} \approx 1$ in ~1500 Torr Ar at ~433 K. The discrepancy in sample conditions may arise from the combined effects of sample temperature uncertainties, collision cross section uncertainties, repetitive excitation modifications of the nonlinear response, and a rough approximation in calculation of the effect of varying beam overlap. The experimental linewidth, peak splitting depth, and peak twist are closely reproduced by calculations at $T = 200$ fs waiting time under these adjusted conditions; such features depend quantitatively on the relationship between the waiting time, dephasing time, and lifetime, but peak twist is purely a coherent transient effect. This calculation of the experimental twist of the split peaks toward the diagonal qualitatively verifies a new prediction of the 3DFT propagation theory that should be robust to the inclusion of alignment and repetitive excitation

effects in a more complete model. With lower repetition rates to eliminate optical pumping, more fully overlapped beams, improved characterization of the sample absorption spectrum, and modeling that includes alignment effects, it appears that quantitative tests of the 3DFT theory against experimental 2DFT spectra with severe propagation distortions will be possible in the coherent transient regime.

Acknowledgement

This material is based upon work supported by the National Science Foundation under Grant No. CHE-1112365. We thank the Center for Revolutionary Solar Photoconversion for funding the computer used for these calculations. The work at JILA was funded by the NSF through the JILA PFC, award number 1125844.

Notes and References

(1) Hybl, J. D.; Albrecht, A. W.; Gallagher Faeder, S. M.; Jonas, D. M. Two-dimensional Electronic Spectroscopy. *Chem. Phys. Lett.* **1998**, *297*, 307–313.

(2) Zhang, W. M.; Chernyak, V.; Mukamel, S. Multidimensional Femtosecond Correlation Spectroscopies of Electronic and Vibrational Excitons. *J. Chem. Phys.* **1999**, *110*, 5011–5028.

(3) Hybl, J. D.; Albrecht Ferro, A.; Jonas, D. M. Two-dimensional Fourier Transform Electronic Spectroscopy. *J. Chem. Phys.* **2001**, *115*, 6606–6622.

(4) Jonas, D. M. Two-Dimensional Femtosecond Spectroscopy. *Annu. Rev. Phys. Chem.* **2003**, *54*, 425–463.

(5) Cundiff, S. T.; Zhang, T.; Bristow, A. D.; Karaiskaj, D.; Dai, X. Optical Two-Dimensional Fourier Transform Spectroscopy of Semiconductor Quantum Wells. *Acc. Chem. Res.* **2009**, *42*, 1423–1432.

(6) Ogilvie, J. P.; Kubarych, K. J. Multidimensional Electronic and Vibrational Spectroscopy: An Ultrafast Probe of Molecular Relaxation and Reaction Dynamics. *Adv. Atom. Mol. Opt. Phys.* **2009**, *57*, 249–321.

(7) Olson, R. W.; Lee, H. W. H.; Patterson, F. G.; Fayer, M. D. Optical Density Effects in Photon Echo Experiments. *J. Chem. Phys.* **1982**, *76*, 31–39.

(8) Spano, F. C.; Warren, W. S. Photon Echo Decays in Optically Dense Media. *J. Chem. Phys.* **1990**, *93*, 1546–1556.

(9) Kinrot, O.; Prior, Y. Nonlinear Interaction of Propagating Short Pulses in Optically Dense Media. *Phys. Rev. A* **1995**, *51*, 4996–5007.

(10) Keusters, D.; Warren, W. S. Propagation Effects on the Peak Profile in Two-dimensional Optical Photon Echo Spectroscopy. *Chem. Phys. Lett.* **2004**, *383*, 21–24.

(11) Belabas, N.; Jonas, D. M. Fourier Algorithm for Four-wave-mixing Signals From Optically Dense Systems With Memory. *Opt. Lett.* **2004**, *29*, 1811–1813.

(12) Belabas, N.; Jonas, D. M. Three-dimensional View of Signal Propagation in Femtosecond Four-wave Mixing With Application to the Boxcars Geometry. *J. Opt. Soc. Am. B* **2005**, *22*, 655–674.

(13) Yetzbacher, M. K.; Belabas, N.; Kitney, K. A.; Jonas, D. M. Propagation, Beam Geometry, and Detection Distortions of Peak Shapes in Two-dimensional Fourier Transform Spectra. *J. Chem. Phys.* **2007**, *126*, 044511.

(14) Cho, B.; Yetzbacher, M. K.; Kitney, K. A.; Smith, E. R.; Jonas, D. M. Propagation and Beam Geometry Effects on Two-Dimensional Fourier Transform Spectra of Multilevel Systems. *J. Phys. Chem. A* **2009**, *113*, 13287–13299.

(15) Cho, B.; Tiwari, V.; Hill, R. J.; Peters, W. K.; Courtney, T. L.; Spencer, A. P.; Jonas, D. M. Absolute Measurement of Femtosecond Pump–Probe Signal Strength. *J. Phys. Chem. A* **2013**, *117*, 6332–6345.

(16) Cho, B.; Tiwari, V.; Jonas, D. M. Simultaneous All-Optical Determination of Molecular Concentration and Extinction Coefficient. *Anal. Chem.* **2013**, *85*, 5514–5521.

(17) Galbán, J.; Marcos, S. d.; Sanz, I.; Ubide, C.; Zuriarrain, J. Uncertainty in Modern Spectrophotometers. *Anal. Chem.* **2007**, *79*, 4763–4767.

(18) Ingle, J. D.; Crouch, S. R. Evaluation of Precision of Quantitative Molecular Absorption Spectrometric Measurements. *Anal. Chem.* **1972**, *44*, 1375–1386.

(19) Ingle, J. D.; Crouch, S. R. *Spectrochemical Analysis*; Prentice Hall: Englewood Cliffs, New Jersey, 1988.

(20) Leo, K.; Wegener, M.; Shah, J.; Chemla, D.; Göbel, E.; Damen, T.; Schmitt-Rink, S.; Schäfer, W. Effects of Coherent Polarization Interactions on Time-resolved Degenerate Four-wave Mixing. *Phys. Rev. Lett.* **1990**, *65*, 1340–1343.

(21) Wegener, M.; Chemla, D.; Schmitt-Rink, S.; Schäfer, W. Line Shape of Time-resolved Four-wave Mixing. *Phys. Rev. A* **1990**, *42*, 5675–5683.

(22) Cundiff, S. T. Time Domain Observation of the Lorentz-local Field. *Laser Phys.* **2002**, *12*, 1073–1078.

(23) Mukamel, S.; Tortschanoff, A. Multiple Quantum Coherences in Liquid State NMR and Nonlinear Optics: Collective vs Local Origin. *Chem. Phys. Lett.* **2002**, *357*, 327–335.

(24) Jeener, J. Comment on 'Multiple Quantum Coherences in Liquid State NMR and Nonlinear Optics: Collective vs Local origin' [Chem. Phys. Lett. 357 (2002) 327]. *Chem. Phys. Lett.* **2003**, *368*, 247–248.

(25) Mukamel, S. Reply to Comment on 'Multiple Quantum Coherences in Liquid State NMR and Nonlinear Optics; Collective vs. Local origin' [Chem. Phys. Lett. 357 (2002) 327]. *Chem. Phys. Lett.* **2003**, *368*, 249–251.

(26) Tortschanoff, A.; Mukamel, S. Collective Many-body Resonances in Condensed Phase Nonlinear Spectroscopy. *J. Chem. Phys.* **2002**, *116*, 5007–5022.

(27) Siegman, A. E. *Lasers*, 1st ed.; University Science Books, 1986.

(28) Albrecht Ferro, A.; Hybl, J. D.; Jonas, D. M. Complete Femtosecond Linear Free Induction Decay, Fourier Algorithm for Dispersion Relations, and Accuracy of the Rotating Wave Approximation. *J. Chem. Phys.* **2001**, *114*, 4649–4656.

(29) Lozovoy, V. V.; Pastirk, I.; Comstock, M. G.; Dantus, M. Cascaded Free-induction Decay Four-wave Mixing. *Chem. Phys.* **2001**, *266*, 205–212.

(30) Garrett, C. G. B.; McCumber, D. E. Propagation of a Gaussian Light Pulse Through an Anomalous Dispersion Medium. *Phys. Rev. A* **1970**, *1*, 305–313.

(31) Fetterman, M. R.; Davis, J. C.; Goswami, D.; Yang, W.; Warren, W. S. Propagation of Complex Laser Pulses in Optically Dense Media. *Phys. Rev. Lett.* **1999**, *82*, 3984–3987.

(32) Weisman, P.; Wilson-Gordon, A. D.; Friedmann, H. Effect of Propagation on Pulsed Four-wave Mixing. *Phys. Rev. A* **2000**, *61*, 053816.

(33) Ziolkowski, R. W.; Judkins, J. B. Applications of the Nonlinear Finite Difference Time Domain (NL-FDTD) Method to Pulse Propagation in Nonlinear Media: Self-focusing and Linear-nonlinear Interfaces. *Radio Sci.* **1993**, *28*, 901–911.

(34) Gruetzmacher, J. A. Correlation Function-based Finite-difference Time-domain Method for Simulating Ultrashort Pulse Propagation. I. Formalism. *J. Chem. Phys.* **2003**, *119*, 1590–1600.

(35) Liu, Q. H. The PSTD Algorithm: A Time-domain Method Requiring Only Two Cells Per Wavelength. *Microw. Opt. Techn. Let.* **1997**, *15*, 158–165.

(36) Butcher, P. N.; Cotter, D. *The Elements of Nonlinear Optics*, 1st ed.; Cambridge Studies in Modern Optics; Cambridge University Press: Cambridge; New York, 1991.

(37) Mukamel, S. *Principles of Nonlinear Optical Spectroscopy*; Oxford Univ. Press: New York, 1995.

(38) Shemetulskis, N. E.; Loring, R. F. Semiclassical Theory of the Photon Echo: Application to Polar Fluids. *J. Chem. Phys.* **1992**, *97*, 1217–1226.

(39) Jansen, T. l. C.; Knoester, J. Waiting Time Dynamics in Two-Dimensional Infrared Spectroscopy. *Acc. Chem. Res.* **2009**, *42*, 1405–1411.

(40) Jansen, T. l. C.; Auer, B. M.; Yang, M.; Skinner, J. L. Two-dimensional Infrared Spectroscopy and Ultrafast Anisotropy Decay of Water. *J. Chem. Phys.* **2010**, *132*, 224503.

(41) Tiwari, V.; Peters, W. K.; Jonas, D. M. Electronic Resonance With Anticorrelated Pigment Vibrations Drives Photosynthetic Energy Transfer Outside the Adiabatic Framework. *Proc. Natl. Acad. Sci. U.S.A.* **2013**, *110*, 1203–1208.

(42) Mukamel, S.; Abramavicius, D. Many-Body Approaches for Simulating Coherent Nonlinear Spectroscopies of Electronic and Vibrational Excitons. *Chem. Rev.* **2004**, *104*, 2073–2098.

(43) Liang, C.; Jansen, T. L. C. An Efficient N^3-Scaling Propagation Scheme for Simulating Two-Dimensional Infrared and Visible Spectra. *J. Chem. Theory Comput.* **2012**, *8*, 1706–1713.

(44) Vöhringer, P.; Arnett, D. C.; Westervelt, R. A.; Feldstein, M. J.; Scherer, N. F. Optical Dephasing on Femtosecond Time Scales: Direct Measurement and Calculation From Solvent Spectral Densities. *J. Chem. Phys.* **1995**, *102*, 4027–4036.

(45) Joo, T.; Jia, Y.; Yu, J.-Y.; Lang, M. J.; Fleming, G. R. Third-order Nonlinear Time Domain Probes of Solvation Dynamics. *J. Chem. Phys.* **1996**, *104*, 6089–6108.

(46) Farrow, D. A.; Yu, A.; Jonas, D. M. Spectral Relaxation in pump–probe Transients. *J. Chem. Phys.* **2003**, *118*, 9348–9356.

(47) Press, W. H.; Teukolsky, S. A.; Vetterling, W.; Flannery, B. *Numerical Recipes in C: The Art of Scientific Computing*, 2nd ed.; Cambridge University Press: Cambridge; New York, 1992.

(48) Seidner, L.; Stock, G.; Domcke, W. Nonperturbative Approach to Femtosecond Spectroscopy: General Theory and Application to Multidimensional Nonadiabatic Photoisomerization Processes. *J. Chem. Phys.* **1995**, *103*, 3998–4011.

(49) Gelin, M. F.; Egorova, D.; Domcke, W. Efficient Method for the Calculation of Time- and Frequency-resolved Four-wave Mixing Signals and Its Application to Photon-echo Spectroscopy. *J. Chem. Phys.* **2005**, *123*, 164112–164112.

(50) Gelin, M. F.; Egorova, D.; Domcke, W. Efficient Calculation of Time- and Frequency-Resolved Four-Wave-Mixing Signals. *Acc. Chem. Res.* **2009**, *42*, 1290–1298.

(51) Rose, T. S.; Wilson, W. L.; Wäckerle, G.; Fayer, M. D. Gas Phase Dynamics and Spectroscopy Probed With Picosecond Transient Grating Experiments. *J. Chem. Phys.* **1987**, *86*, 5370–5391.

(52) Salcedo, J. R.; Siegman, A. E.; Dlott, D. D.; Fayer, M. D. Dynamics of Energy Transport in Molecular Crystals: The Picosecond Transient-grating Method. *Phys. Rev. Lett.* **1978**, *41*, 131–134.

(53) Bosshard, C. Cascading of Second-Order Nonlinearities in Polar Materials. *Adv. Mater.* **1996**, *8*, 385–397.

(54) Meredith, G. R. Second-order Cascading in Third-order Nonlinear Optical Processes. *J. Chem. Phys.* **1982**, *77*, 5863–5871.

(55) Shen, Y. R. *The Principles of Nonlinear Optics*; Wiley-Interscience: New York, 1984.

(56) Siddons, P.; Adams, C. S.; Ge, C.; Hughes, I. G. Absolute Absorption on Rubidium D Lines: Comparison Between Theory and Experiment. *J. Phys. B: At. Mol. Opt.* **2008**, *41*, 155004.

(57) Li, H.; Spencer, A. P.; Kortyna, A.; Moody, G.; Jonas, D. M.; Cundiff, S. T. Pulse Propagation Effects in Optical 2D Fourier-Transform Spectroscopy: Experiment. *J. Phys. Chem. A* **2013**, *117*, 6279–6287.

(58) Lewis, E. Collisional Relaxation of Atomic Excited States, Line Broadening and Interatomic Interactions. *Phys. Rep.* **1980**, *58*, 1–71.

(59) Broadening due to Rb–Ar collisions is calculated from eq 6.1 of ref 58 using the pressure-broadening coefficient reported by Rotondaro and Perram[87].

(60) Dai, X.; Bristow, A. D.; Karaiskaj, D.; Cundiff, S. T. Two-dimensional Fourier-transform Spectroscopy of Potassium Vapor. *Phys. Rev. A* **2010**, *82*, 052503.

(61) Allen, L.; Eberly, J. H. *Optical Resonance and Two-Level Atoms*; Dover: New York, 1987.

(62) Stamper, J. H. Quenching of Na Radiation by He. *J. Chem. Phys.* **1965**, *43*, 759–760.

(63) Copley, G.; Kibble, B. P.; Krause, L. Experimental Evidence for the Absence of Quenching of Sodium Resonance Radiation by Inert Gases. *Phys. Rev.* **1967**, *163*, 34–35.

(64) Bellisio, J. A.; Davidovits, P.; Kindlmann, P. J. Quenching of Rubidium Resonance Radiation by Nitrogen and the Noble Gases. *J. Chem. Phys.* **1968**, *48*, 2376–2377.

(65) Edwards, M. G. The Quenching of Alkali Fluorescence by Rare Gases. *J. Phys. B: At. Mol. Phys.* **1969**, *2*, 719–722.

(66) Lijnse, P. L.; Zeegers, P. J. T.; Alkemade, C. T. J. Electronic-excitation Transfer Collisions in Flames-III: Cross Sections for Quenching and Doublet Mixing of Rb($5^2P_{3/2,\,1/2}$) Doublet by N_2, O_2, H_2 and H_2O. *J. Quant. Spectrosc. Radiat. Transfer* **1973**, *13*, 1033–1045.

(67) Gallagher, A. Collisional Depolarization of the Rb 5p and Cs 6p Doublets. *Phys. Rev.* **1967**, *157*, 68–72.

(68) Gallagher, A. Collisional Depolarization of the Rb 5p and Cs 6p Doublets (Erratum). *Phys. Rev.* **1967**, *163*, 206–206.

(69) Fourkas, J. T.; Fayer, M. D. The Transient Grating: A Holographic Window to Dynamic Processes. *Acc. Chem. Res.* **1992**, *25*, 227–233.

(70) Williams, S.; Zare, R. N.; Rahn, L. A. Reduction of Degenerate Four-wave Mixing Spectra to Relative Populations I. Weak-field Limit. *J. Chem. Phys.* **1994**, *101*, 1072–1092.

(71) Williams, S.; Rahn, L. A.; Zare, R. N. Effects of Different Population, Orientation, and Alignment Relaxation Rates in Resonant Four-wave Mixing. *J. Chem. Phys.* **1996**, *104*, 3947–3955.

(72) Tokmakoff, A. Orientational Correlation Functions and Polarization Selectivity for Nonlinear Spectroscopy of Isotropic Media. I. Third Order. *J. Chem. Phys.* **1996**, *105*, 1–12.

(73) Condon, E. U.; Shortley, G. H. *The Theory of Atomic Spectra*, reprinted with corrections ed.; Cambridge University Press: Cambridge, 1957.

(74) Townes, C. H. *Microwave Spectroscopy*; Dover: New York, 1975.

(75) Qian, W.; Jonas, D. M. Role of Cyclic Sets of Transition Dipoles in the pump–probe Polarization Anisotropy: Application to Square Symmetric Molecules and Perpendicular Chromophore Pairs. *J. Chem. Phys.* **2003**, *119*, 1611–1622.

(76) Using the M_J state to M_J state transition dipoles for the $^2S_{1/2}$ to $^2P_{3/2}$ fine structure transition calculated from the LS coupling spin-orbit wavefunctions given by eq 8b on page 123 of ref 73 and the direction cosine matrix elements in Table 4-4 of ref 74 to calculate the coherent pump–probe polarization anisotropy[75] yields $r = 1/6$, indicating that the initial amplitude of the alignment response is one-third that of the population response.

(77) Happer, W. Optical Pumping. *Rev. Mod. Phys.* **1972**, *44*, 169–249.

(78) Quack, M., Merkt, F., Eds. *Handbook of High-Resolution Spectroscopy*; Wiley: Chichester, West Sussex, 2011; Vol. 1.

(79) Reitz, J. R.; Milford, F. J.; Christy, R. W. *Foundations of Electromagnetic Theory*, 4th ed.; Addison-Wesley: Reading, Mass., 1993.

(80) Gallagher, S. M.; Albrecht, A. W.; Hybl, J. D.; Landin, B. L.; Rajaram, B.; Jonas, D. M. Heterodyne Detection of the Complete Electric Field of Femtosecond Four-wave Mixing Signals. *J. Opt. Soc. Am. B* **1998**, *15*, 2338–2345.

(81) Bracewell, R. N. *The Fourier Transform and Its Applications*, 3rd ed.; McGraw-Hill Series in Electrical and Computer Engineering; McGraw Hill: Boston, 2000.

(82) Gallagher Faeder, S. M.; Jonas, D. M. Two-Dimensional Electronic Correlation and Relaxation Spectra: Theory and Model Calculations. *J. Phys. Chem. A* **1999**, *103*, 10489–10505.

(83) Equation 31 is related to the propagation function for two-beam double-resonance experiments given immediately below eq 60 of ref 12 except for two differences. First, β is not required to be zero in eq 31. Second, a factor of γ arising from κ_z in the denomenator of eq 30 is present in eq 31 but is missing in eq 60 of ref 12.

(84) Bracewell, R. Strip Integration in Radio Astronomy. *Aust. J. Phys.* **1956**, *9*, 198–217.

(85) Brand names are given as technical information only and does not imply endorsement by NIST or that the product is the best for the purpose.

(86) *International Mathematics and Statistics Library (IMSL)*, version 6.0; Fortran Numerical Library; Visual Numerics: Houston, TX, 2006.

(87) Rotondaro, M. D.; Perram, G. P. Collisional Broadening and Shift of the Rubidium D_1 and D_2 Lines ($5^2S_{1/2} \rightarrow 5^2P_{1/2}$, $5^2P_{3/2}$) by Rare Gases, H_2, D_2, N_2, CH_4 and CF_4. *J. Quant. Spectrosc. Radiat. Transfer* **1997**, *57*, 497–507.

(88) Ottinger, C.; Scheps, R.; York, G. W.; Gallagher, A. Broadening of the Rb Resonance Lines by the Noble Gases. *Phys. Rev. A* **1975**, *11*, 1815–1828.

(89) Weller, L.; Bettles, R. J.; Siddons, P.; Adams, C. S.; Hughes, I. G. Absolute Absorption on the Rubidium D_1 Line Including Resonant dipole–dipole Interactions. *J. Phys. B: At. Mol. Opt.* **2011**, *44*, 195006.

(90) Allard, N.; Kielkopf, J. The Effect of Neutral Nonresonant Collisions on Atomic Spectral Lines. *Rev. Mod. Phys.* **1982**, *54*, 1103–1182.

(91) Demtröder, W. *Laser Spectroscopy: Vol. 1: Basic Principles*, 4th ed.; Springer: Berlin, 2008.

(92) Lorenz, V. O.; Cundiff, S. T. Non-Markovian Dynamics in a Dense Potassium Vapor. *Phys. Rev. Lett.* **2005**, *95*, 163601.

(93) Lorenz, V. O.; Cundiff, S. T. Ultrafast Spectroscopy of a Dense Potassium Vapor. *Chem. Phys.* **2007**, *341*, 106–112.

(94) Lorenz, V. O.; Mukamel, S.; Zhuang, W.; Cundiff, S. T. Ultrafast Optical Spectroscopy of Spectral Fluctuations in a Dense Atomic Vapor. *Phys. Rev. Lett.* **2008**, *100*, 013603.

(95) Steck, D. A. *Rubidium 85 D Line Data*; 2012; available online at http://steck.us/alkalidata (revision 2.1.5, 19 September 2012).

(96) Kondo, R.; Tojo, S.; Fujimoto, T.; Hasuo, M. Shift and Broadening in Attenuated Total Reflection Spectra of the Hyperfine-structure-resolved D_2 Line of Dense Rubidium Vapor. *Phys. Rev. A* **2006**, *73*, 062504.

(97) Alcock, C. B.; Itkin, V. P.; Horrigan, M. K. Vapour Pressure Equations for the Metallic Elements: 298–2500K. *Can. Metall. Quart.* **1984**, *23*, 309–313.

(98) Shang-Yi, C. Pressure Effects of Homogeneous Rubidium Vapor on Its Resonance Lines. *Phys. Rev.* **1940**, *58*, 884–887.

(99) Nesmeyanov, A. N. *Vapor Pressure of the Chemical Elements*; Elsevier Pub. Co: Amsterdam, New York, 1963.

(100) Izotova, S. L.; Kantserov, A. I.; Frish, M. S. Constants for Broadening and Shift of D_1 and D_2 Rubidium-87 Lines by Inert Gases. *Opt. Spectrosc.* **1981**, *51*, 107–109.

(101) Kantor, P. Y.; Shabanova, L. N. Profiles of the Rb I 794.7- and 780.0-nm Lines in the Presence of Inert Gases; Parameters of Interatomic Potentials. *Opt. Spectrosc.* **1985**, *58*, 614–619.

(102) Granier, R. Study of Influence of Atomic Interactions on Shape of Spectral Rays. *Ann. Phys.-Paris* **1969**, *4*, 383–&.

(103) Granier, R.; Granier, J.; Schuller, F. Calculations of Impact Broadening and Shift of Spectral Lines for Realistic Interatomic Potentials. *J. Quant. Spectrosc. Radiat. Transfer* **1976**, *16*, 143–146.

(104) Lorenz, V. O.; Dai, X.; Green, H.; Asnicar, T. R.; Cundiff, S. T. High-density, High-temperature Alkali Vapor Cell. *Rev. Sci. Instrum.* **2008**, *79*, 123104.

(105) Bouchiat, M. A.; Guéna, J.; Jacquier, P.; Lintz, M.; Papoyan, A. V. Electrical Conductivity of Glass and Sapphire Cells Exposed to Dry Cesium Vapor. *Appl Phys B* **1999**, *68*, 1109–1116.

(106) Berman, P. R.; Lamb, W. E. Influence of Resonant and Foreign Gas Collisions on Line Shapes. *Phys. Rev.* **1969**, *187*, 221–266.

(107) The mean time between Rb–Ar collisions is calculated using $\bar{\tau} \approx (N\pi b_0^2 v)^{-1}$ given just above eq 1a by Berman and Lamb [106] where N is the number density of perturber (Ar) atoms, b_0 is the critical impact parameter defined so that $\sigma_R = \pi b_0^2$, and v is the mean relative speed between chromophore (Rb) and perturber (Ar) atoms. The mean time between collisions can be expressed as $\bar{\tau} \approx (N\sigma_R v)^{-1}$ where σ_R is the collisional cross section for (Rb–Ar) optical line broadening. In

Table 6.2, Lewis[58] lists three experimental measurements of σ_R for the Rb D_2 line and the mean of these three values (330×10^{-16} cm^2) was used here for σ_R. The collision duration was calculated using $\tau_c = b_0/v$ given just above eq 1a by Berman and Lamb.[106]

(108) Fox, C. D. Radial Distribution of Absorption in a Cesium Heat Pipe With Axial Laser Heating. Master of Science Thesis, Air Force Institute of Technology, Wright-Patterson Air Force Base, Ohio, 2011.

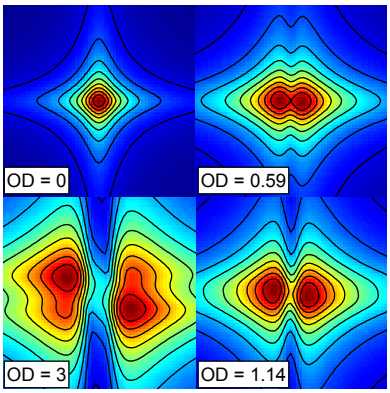

For Table of Contents Only.